Growth Mechanisms and Tribocorrosion Behavior of Bio-Functionalized ZrO$_2$ Nanoparticles-Containing MAO Coatings Formed on Ti-40Nb Alloy

N. A. Costa[1,2] · A. L. Rossi[3] · A. C. Alves[4] · A. M. P. Pinto[4,5] · F. Toptan[4,5] · L. A. Rocha[1,2,4]

Abstract

Tribocorrosion resistance, low elastic modulus, and faster promotion of osseointegration are among the current requirements to avoid aseptic loosening in artificial joints. Therefore, in this work, a promising orthopedic Ti-40Nb alloy was used and its surface was modified by micro-arc oxidation (MAO), resulting in a multi-scale porous surface incorporated with multiple bioactive species (Ca, P, Mg, Zn, and Sr) and ZrO$_2$ nanoparticles (ZrO$_2$ NPs). The effect of different processing voltages is discussed on the formation mechanisms of the coatings and incorporation of ZrO$_2$ NPs. The resulting tribocorrosion behavior is elucidated for two loading conditions in phosphate-buffered saline (PBS) solution. Similar growth mechanisms were observed for all films, resulting in a triplex structure (barrier film, inner porous layer, and outer porous layer). However, higher processing voltage produced thicker anodic films with smaller average surface porosity and increased rutile content. Higher voltage also resulted in higher amounts of ZrO$_2$ NPs in the coating. A mechanism is proposed to explain the incorporation of NPs, based on the combined effect of electrophoresis and strong micro-arcs and discharges originated during MAO treatment. That enhanced incorporation of ZrO$_2$ NPs may retard eventual phenomena of cracking associated with harder materials (rutile) under vigorous mechanical solicitations.

Keywords Orthopedic implant · Ti-40Nb alloy · Micro-arc oxidation · Nanoparticle incorporation · Tribocorrosion

1 Introduction

Knee and hip are articulations significantly affected by bone degenerating diseases, namely osteoarthritis and osteoporosis, leading to a growing demand for total joint replacements [1–3]. The artificial joint devices' lifespan depends

✉ N. A. Costa
n.costa@unesp.br

1 Faculdade de Ciências, UNESP–Universidade Estadual Paulista, Bauru, SP 17033-360, Brazil

2 IBTN/Br–Brazilian Branch of the Institute of Biomaterials, Tribocorrosion and Nanomedicine, Bauru, SP 17033-360, Brazil

3 CBPF–Brazilian Center for Research in Physics, Rio de Janeiro, RJ 22290-180, Brazil

4 CMEMS-UMinho–Center of MicroElectroMechanical Systems-Universidade do Minho, 4800-058 Azurém, Guimarães, Portugal

5 Department of Mechanical Engineering, University of Minho, 4800-058 Azurém, Guimarães, Portugal

on several factors, from the surgical technique to the complex interactions between implant, surrounding bone, and patient's organism. After surgery, aseptic loosening has been widely reported as one of the main complications by prosthesis-associated factors [4–6]. It can be originated from excessive wear of articular surfaces, biomechanical mismatch between bone and implant, and relative micromotion effect [7, 8].

The process of wear in total joint replacements can occur at their articular surfaces due to relative movements between implant and adjacent bone during physiological cyclic loads. The deterioration of the material may be aggravated by combining the harsh biological environment's actions due to the presence of corrosive body fluids. The simultaneous action of wear and corrosion is defined as tribocorrosion. Under tribological conditions, it is well known that the wear and corrosion mechanisms can be intensified by each other, resulting in a total material loss significantly higher as compared to that by individual wear or corrosion damages [7, 9–11]. Furthermore, a critical consequence of excessive wear is the release of wear debris to the surrounding environment.

Wear debris may lead to macrophages (inflammatory cells) to secrete cytokines and chemokines that induce osteoclastogenesis with consequent bone resorption [4].

Another major clinical problem discussed by current studies is the large difference in Young's modulus between bone (10–30 GPa) and the currently available Ti-based implant materials (commercially pure Ti: 110 GPa, Ti-6Al-4V: 114 GPa) [12, 13]. This biomechanical mismatch decreases stress distribution at the bone–implant interface (a phenomenon known as stress shielding), which results in bone resorption due to the lack of mechanical stimulation needed for bone development [14, 15].

Also identified as a cause of aseptic loosening, the micromotion effect can be induced by poor osseointegration [7], a fundamental bone formation process strongly dependent on the implant material's surface properties [16, 17].

To overcome the significant clinical concerns above referred, various studies have been devoted to developing novel β and near β-type Ti alloys (mainly due to their promising low elastic modulus). Besides, multiple surface treatments have been proposed to enhance tribocorrosion performance and bioactivity, also avoiding other issues such as bacteria adhesion [13, 18, 19].

Alloys from the binary Ti–Nb system have been under special attention. In fact, a positive in vitro interaction with osteoblastic cells may qualify Nb as a promising alloying element for Ti alloys [20]. As Nb is a strong β-stabilizing element, this phase can be retained from 30% in weight of Nb in bulk, resulting in Ti alloys with low elastic modulus [13, 21]. Additionally, β-type TiNb alloys have demonstrated high corrosion resistance by forming a TiO_2 and Nb_2O_5 passive layer on the metallic surface [22].

Among the modified surfaces of Ti, micro-arc oxidation (MAO)-treated coatings have excellent corrosion and tribocorrosion resistance through the porous Ti oxide layers with both anatase and rutile phases [23–27]. The bioactive agents such as Ca and P [28–30], Zn [31], Mg [27], and Sr [32–35] incorporated into those anodic films also provide favorable biological behavior at the bone–implant interface. It can be found in the literature that it is also possible to bio-functionalize Ti–Nb alloys using MAO treatments [36], although joint incorporation of the mentioned bioactive elements is still not reported.

Due to its great versatility, the MAO technique can be coupled with electrophoretic deposition to incorporate particles (nm or μm scale) into the oxide films. Their incorporation mode (inert, partial, or reactive) depends on numerous parameters, including voltage used during the process, which is capable of modifying electrophoretic forces and discharge events. On the other hand, the type of incorporation seems to affect the tribological properties in different ways. It is considered that the wear protection can be increased by adding hard particles (inert incorporation) or forming new phases with high hardness (reactive incorporation) in the anodic coatings [37, 38]. In this view, electrolytes with ZrO_2 particles have been largely employed to fabricate MAO coatings with improved wear and corrosion resistance. Studies on the incorporation of such particles have involved different substrate materials, such as Mg and its alloys [39–45], Al and its alloys [46–49], and also pure Ti [38, 50, 51] and Ti-6Al-4V alloy [52]. Nevertheless, there is a lacking of investigation on the formation of ZrO_2 particles-incorporated MAO coatings on β-type Ti alloys, and consequently, their tribocorrosion degradation mechanism is poorly understood.

Thus, this work aimed to be the first insight on the growth mechanisms and tribocorrosion behavior of bio-functionalized ZrO_2 nanoparticles-containing MAO coatings formed on Ti-40Nb alloy. The substrates of 40% in weight of Nb were chosen due to their low Young's modulus (62 ± 7 GPa [53]). Joint incorporation of Ca, P, Zn, Mg, and Sr was considered to bio-functionalize the MAO-treated coatings. Two different voltages were applied during anodic treatments to evaluate their influence on the formation mechanisms of the coatings and incorporation of the ZrO_2 nanoparticles. Furthermore, the resulting tribocorrosion behavior of the oxide films is finally elucidated.

2 Material and Methods

2.1 Preparation of the Alloy

Commercially pure titanium (grade 2; Sandinox) and niobium (99.8% purity; Companhia Brasileira de Metalurgia e Mineração, CBMM) were used as precursor materials. Initially, the metals were etched in acidic solution [1:4 ($V_{HF} : V_{HNO_3}$) for Ti, and 2:2:1 ($V_{HF} : V_{HNO_3} : V_{H_2O}$) for Nb], ultrasonically cleaned in acetone for 15 min, and then dried with warn air. Ingots of the Ti-40Nb (wt%) alloy were produced by an arc-melting furnace composed of non-consumable tungsten electrode, water-cooled copper crucible, and controlled argon atmosphere. The ingots were re-melted for five times to provide homogeneity.

2.2 MAO Processing

As-cast Ti-40Nb samples were bio-functionalized by MAO treatment using electrolyte composition of 0.35 M calcium acetate monohydrate (CaA), 0.02 M β-glycerophosphate disodium salt pentahydrate (β-GP), 0.1 M magnesium acetate tetrahydrate (MgA), 0.02 M zinc acetate dihydrate (ZnA), and 0.04 M strontium acetate (SrA) (reagents from Sigma-Aldrich), with and without the addition of 9 g/L ZrO_2 nanoparticles (ZrO_2 NPs) (size of 40–60 nm; acquired doped by 3 mol% Y_2O_3, TOSOH). All electrolyte compositions showed pH level of 7.3–7.4. Prior to the treatment,

the samples were polished till #800 grit SiC waterproof paper and cleaned in propanol for 10 min in ultrasonic bath, followed by chemical etching in Kroll's reagent solution (2:10:88 in vol. of HF, HNO$_3$ and H$_2$O, respectively) during 30 s, then sonication in propanol (10 min) and distilled water (5 min). Using a DC power supply (Keysight Technologies N5772A), each MAO treatment was carried out at room temperature during 1 min, with a limiting current of 2.5 A. To investigate the influence of the voltage on ZrO$_2$ NPs incorporation, values of 300 and 400 V were chosen to be applied between the samples (anode) and a pure Ti (grade 2) plate (cathode). A distance of about 7 cm was kept between electrodes. The MAO treatment (depicted in Fig. 1) was done in triplicate, under magnetic agitation (500 rpm). After the treatment, the samples were rinsed with distilled water and propanol and then dried with warm air. The samples were named according to Table 1.

2.3 Surface and Cross-Section Characterization of the Porous TiO$_2$ Films

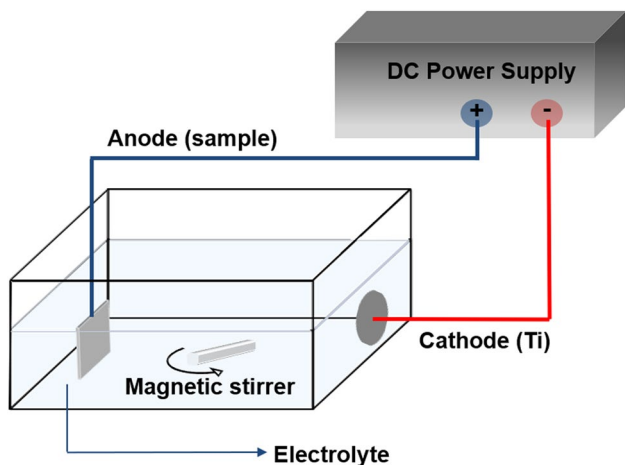Surface of the MAO-treated coatings was investigated by field emission gun scanning electron microscopy

(FEG-SEM) (TESCAN LYRA 3) and energy-dispersive X-ray spectroscopy (EDS) (Oxford Instruments). Average surface porosity (% of area occupied by pores) was measured by ImageJ software. Three SEM images were processed for each sample representing three different zones of the surface, and three samples were examined per group. Cross-section of the samples was obtained by using a dual beam instrument equipped with focused ion beam (FIB) (TESCAN LYRA 3), operating a Ga$^+$ ion source. To protect the samples from unnecessary sputtering, a Pt layer was locally deposited in situ through a gas injection system and 0.2 nA Ga$^+$ ion current accelerated at 30 keV. To reveal the substrate–film interface, bulk etching was performed with 5 nA, and fine milling (polishing) was performed on the edge of the trenches with 1 nA, both at 30 keV. Structural characteristics of the coatings were evaluated by X-ray diffraction (XRD) (PANalytical X'Pert PRO X-Ray), operating at 40 kV and 40 mA, CuKα radiation ($\lambda = 0.15405$ nm), spinner mode with revolution time of 4 s, scan ranging from 20° to 60° (2θ) with steps of 0.0334° and a counting time of 10 s/step. Peaks data were recorded by X'Pert Data Collector software. XRD patterns were indexed using Inorganic Crystal Structure Database (ICSD) (card numbers: anatase #9852, rutile #33837, tetragonal-phase zirconia #66781, and β-phase titanium #44391). The phase percentage was calculated using the following Eq. (1):

$$\%\text{Phase}_\alpha = \frac{\sum I_{\alpha\text{peaks}}}{\sum I_{\text{all peaks}}} \tag{1}$$

2.4 Tribocorrosion Tests

For the tribocorrosion experiments, samples were fixed in a tribo-electrochemical cell and mounted on a ball-on-disk reciprocating sliding tribometer (CETR-UMT-2) (Fig. 2). The cell was filled by the electrolyte with the testing surface area facing upwards. A two-electrode setup was used, considering samples as working electrode and a saturated Ag/AgCl electrode as reference electrode. To simulate human body conditions, the electrolyte consisted
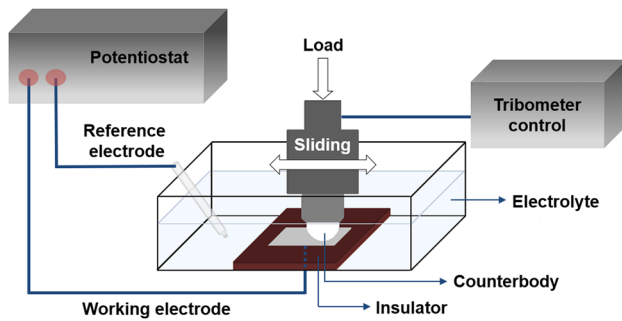

Fig. 1 Schematic illustration of the MAO treatment setup

Table 1 Groups of samples and their respective treatment condition

Group	Electrolyte composition						Potential applied (V)
	CaA (M)	β-GP (M)	MgA (M)	ZnA (M)	SrA (M)	ZrO$_2$ NPs (g/L)	
TiNb	Etched samples (without MAO treatment)						–
TiNb0-300	0.35	0.02	0.1	0.02	0.04	–	300
TiNb0-400	0.35	0.02	0.1	0.02	0.04	–	400
TiNb9-300	0.35	0.02	0.1	0.02	0.04	9	300
TiNb9-400	0.35	0.02	0.1	0.02	0.04	9	400

Fig. 2 Schematic diagram of the tribocorrosion tests setup

of phosphate-buffered saline (PBS) solution (8 g/L NaCl, 0.2 g/L KCl, 0.24 g/L KH_2PO_4, and 1.44 g/L Na_2HPO_4 in distilled water, with adjusted pH of 7.4) at 37 ± 2 °C. Alumina balls (10 mm diameter; Ceratec) were used as counter-body to slide for 30 min on the samples surface, with linear stroke amplitude of 3 mm, and frequency of 1 Hz. The degradation mechanism of the samples was assessed by applying two different normal loads: 2 and 3 N, corresponding to maximum Hertzian contact pressures of approx. 370 and 430 MPa, respectively, for the untreated Ti-40Nb alloy, in order to assume mechanical solicitations significantly higher compared to the ones reported for both hip (between approx. 3 and 9 MPa) [54] and knee (between approx. 2 and 32 MPa) [55] implants, but still not exceeding the yield strength of dense Ti-40Nb substrates (around 544 ± 66 MPa) [53]. Open circuit potential (OCP) was monitored until stabilization (ΔE bellow 60 mV/h), during the whole 1800 cycles of sliding, and also after the mechanical actions, for 30 min, using a potentiostat Gamry Reference 600 coupled to Gamry framework software. The coefficient of friction (COF) was calculated through the tangential forces recorded during sliding by UMT-2 software coupled to the tribometer. To ensure repeatability of the results, at least three samples of each treatment condition were tested. After tribocorrosion tests, samples were ultrasonically cleaned in propanol for 15 min, followed by 10 min in distilled water, and finally rinsed with propanol and dried with warm air.

2.5 Characterization of the Worn Surfaces

Morphology and elemental composition of the worn surfaces were assessed by FEG-SEM (FEI Nova 200) and EDS (Pegasus X4M). The sub-surface damage of the films was evaluated by FEG-SEM, with the support of FIB to obtain the cross-section (TESCAN LYRA 3) using the same procedure previously referred in Sect. 2.3.

3 Results

3.1 As-Processed Surfaces

Top-view SEM images of the as-functionalized samples are given in Fig. 3. A typical multi-scale (nm and μm) porous structure was obtained for all samples, but some differences in morphology can be observed when the voltage of the anodic treatment was changed. For the 400 V-treated groups, various cracks propagating through small pores are visible throughout the surface (Fig. 3b, d). By adding ZrO_2 NPs into the electrolyte, the coatings were decorated by light regions corresponding to tiny particles and agglomerates of such particles (Fig. 3c, d). As indicated by the dotted arrows in the backscattered electron (BSE) images, the numerous ZrO_2 NPs were found protruded or embedded in the coating surface, as well as inside the pores or cracks, regardless of the voltage value. The average surface porosity (% of area occupied by pores) showed distinct values between TiNb0-300 (7.5%) and TiNb9-300 (7.1%) samples. On the other hand, MAO processing at higher voltage led to smaller porosity, with value of 5.3% for the TiNb0-400 coatings, and significant decrease for 3.3% when the coating was treated with ZrO_2 NPs (TiNb9-400).

Figure 4 gives a representative EDS mapping of the surface of each coating (with and without nanoparticles). The presence of Ti, Nb, and O was identified for all coatings. TiNb0-300 and TiNb0-400 samples (represented in Fig. 4a) showed elements Ca, P, Mg, Zn, and Sr uniformly distributed over the surface. The successful incorporation of these bioactive species can be also seen for the coatings treated with ZrO_2 NPs (TiNb9-300 and TiNb9-400 samples represented in Fig. 4b). Regions containing brighter zones on the micrographs of Fig. 3c, d exhibited a higher concentration of Zr in the EDS analysis, which reinforces an agglomeration of ZrO_2 NPs in these sites. On the other hand, P atoms seem to be agglomerated at the same regions probably due to the proximity between the P Kα (2013 eV) and the Zr Lα (2042 eV) peaks in the EDS spectrum.

Figure 5 presents the cross-sectional FIB-SEM micrographs of the as-functionalized samples. Three main layers are revealed for all coatings. At the metal/oxide interface, there is a compact and thin layer which is recognized as barrier film (A). The following two layers are characterized by pores: an inner porous layer having small pores (B), whereas the outer porous layer mostly presents larger pores (C) [23, 56]. From these cross-sectional images, the presence of cracks could be more evident as the voltage increased to 400 V (Fig. 5b, d). Regarding the coatings treated with zirconia (Fig. 5c, d),
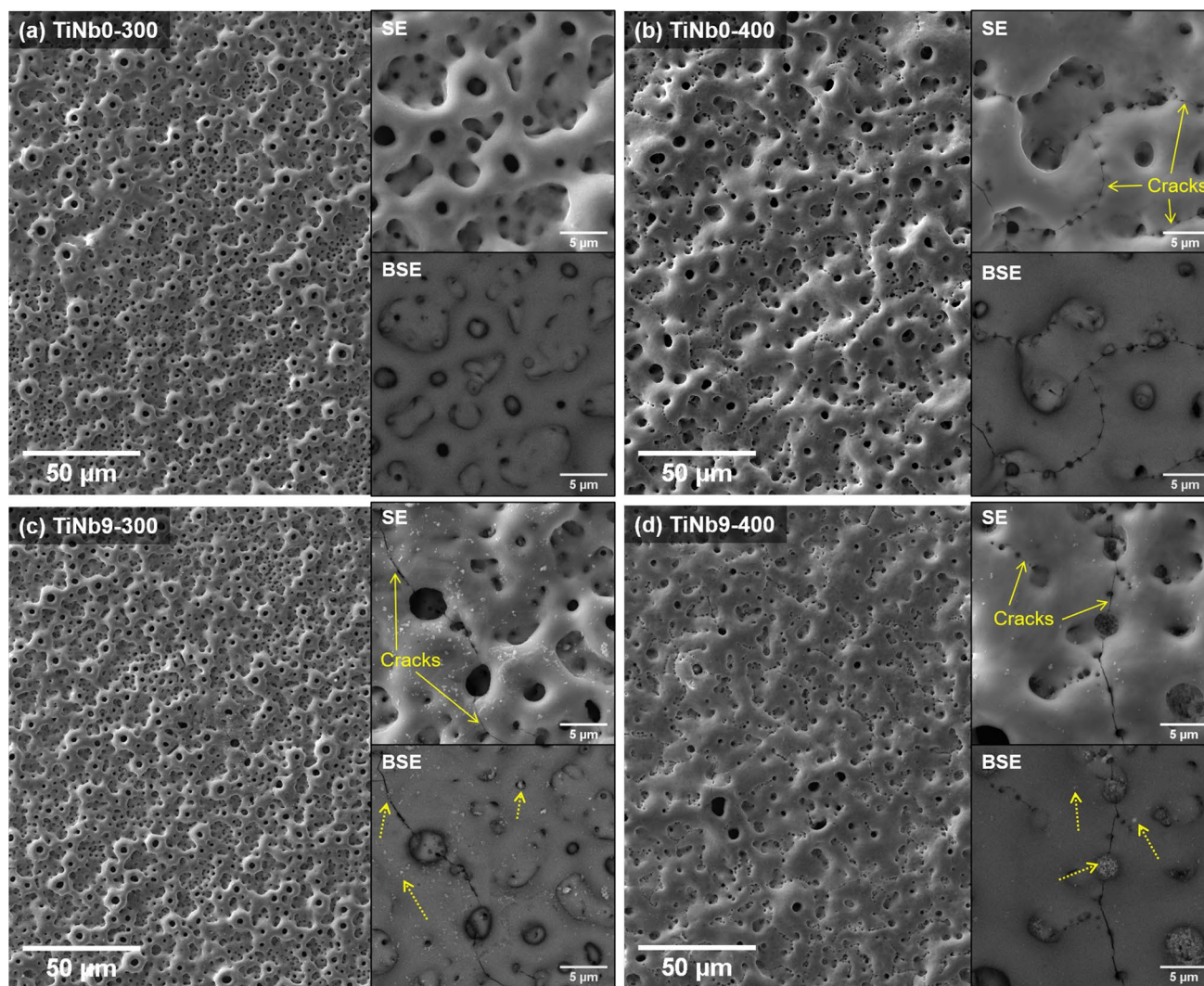
Fig. 3 Surface SEM micrographs of the **a** TiNb0-300, **b** TiNb0-400, **c** TiNb9-300, and **d** TiNb9-400 coatings. Inset images represent areas at higher magnification in both backscattered electron (BSE) and secondary electron (SE) modes. ZrO$_2$ NPs indicated by dotted arrows

those ceramic nanoparticles were identified above the barrier film (mainly layers C) by brighter regions in the BSE images (marked by the dotted arrows). The cross-section of the TiNb9-300 samples showed embedded nanoparticles, whereas pores and cracks of the TiNb9-400 coating, were also well-distinguished sites for the incorporation of ZrO$_2$ NPs. The waved topography of the oxide layers can be responsible for a large variation in thickness [27]. From these cross-sectional images, the thickness was estimated ranging from 5–7 to 6–8 µm for the TiNb0-300 and TiNb9-300 coatings, respectively. For the coatings grown at 400 V, the thickness was significantly higher, within the ranges of 11–13 and 10–16 µm for TiNb0-400 and TiNb9-400 samples, respectively.

XRD spectra obtained on the samples are given in Fig. 6. All coatings presented a mixture of crystalline structures of anatase and rutile (TiO$_2$). The presence of peaks of zirconia in its tetragonal phase (t-ZrO$_2$) is another indicative of ZrO$_2$ NPs incorporated into the TiNb9-300 and TiNb9-400 coatings. A characteristic shoulder of amorphous phase is detected within the range between 25° and 37° (2θ) for both 400 V-treated groups. It is also observed a significative increase in the rutile to anatase ratio (R/A) at higher voltage (400 V) applied during MAO treatment, with R/A equal to 0.29 and 0.35 for the TiNb0-300 and TiNb9-300 samples, respectively, and R/A equal to 0.95 and 1.11 for the TiNb0-400 and TiNb9-400 coatings, respectively. In addition, these results indicated that the presence of ZrO$_2$ NPs in the electrolyte also seems to favor the formation of rutile, especially for the TiNb9-400 samples. Concerning the crystalline ZrO$_2$/TiO$_2$ ratio, the values of 0.10 and 0.13 were measured for the TiNb9-300 and TiNb9-400 coatings, respectively.
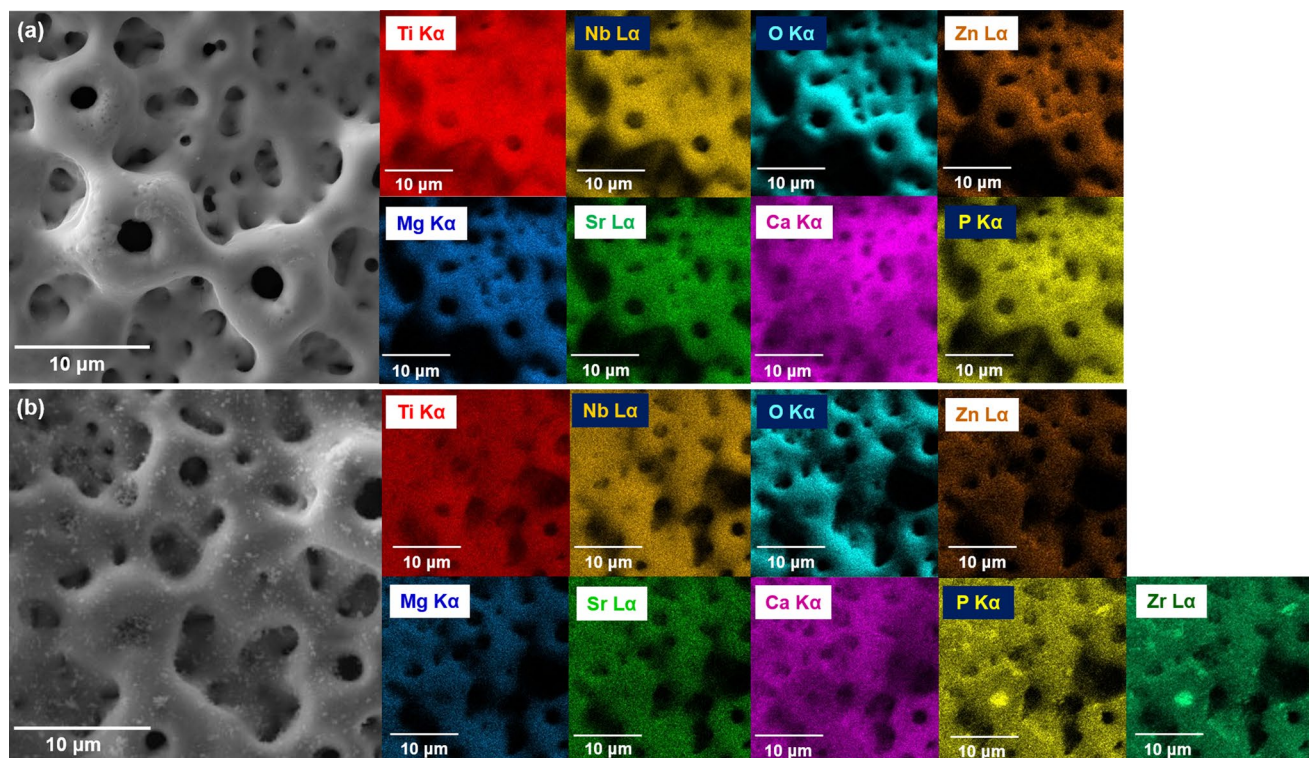
Fig. 4 Representative EDS mapping of the coatings **a** not treated (TiNb0-300 and TiNb0-400) and **b** treated (TiNb9-300 and TiNb9-400) with ZrO_2 NPs

3.2 Characterization After Tribocorrosion Experiments

3.2.1 Normal Load: 2 N

Figure 7 represents the tribo-electrochemical response of the MAO-treated groups and the untreated Ti-40Nb alloy samples, through evolution of OCP before, during, and after sliding under 2 N normal load, as well as the evolution of their respective COF values recorded throughout the mechanical solicitations.

Before sliding, the MAO-treated groups showed OCP significantly nobler comparing to the one recorded on the untreated TiNb samples, indicating that the growth of anodic coating could decrease the corrosion susceptibility [27].

As soon as the counter-body starts to move, an abrupt potential drop is noticed for the untreated TiNb samples, which suggests destruction of the passive oxide layer and consequent exposure of the bare titanium alloy to the corrosive physiological environment [27, 57]. During the successive contact events by sliding, these metallic samples showed OCP values of around $-0.70\ V_{Ag/AgCl}$, accompanied by some small oscillations generally related to phenomena of mechanical depassivation and electrochemical repassivation [27, 58]. Once sliding is interrupted, the OCP exhibits an anodic shift, reaching similar level as observed before

starting the mechanical actions, which may indicate recovery of the passive film on the wear track region [10].

For each MAO-treated coating, there is no significant difference in the electrochemical behavior throughout the test. These stable OCP values suggest increased wear resistance for the coated samples, regardless of their MAO processing parameters.

Regarding the COF evolution during sliding, the untreated TiNb samples kept a relatively stable value around 0.7 during the whole period of mechanical solicitations. However, distinctive COF measurements are observed for the MAO-treated coatings. In the case of the TiNb0-300 samples, as soon as the sliding begins the COF stabilizes around 0.35, increasing at a very gradual rate in the next moments till reach around 0.45. After that, it is observed a small but fast increase in the COF values to approximately 0.5. A similar behavior in the COF is seen between both TiNb0-400 and TiNb9-300 samples, presenting COF values ranging between 0.45 and 0.5 after the initial sliding stage. In respect to TiNb9-400 samples, after the first moments of the running-in period, the COF values remain relatively stable around 0.55 till the end of sliding. Although some of the COF values have been changed, they still remained much lower than the one recorded for the untreated TiNb samples, which means that the sliding mainly took place between the alumina sphere and the
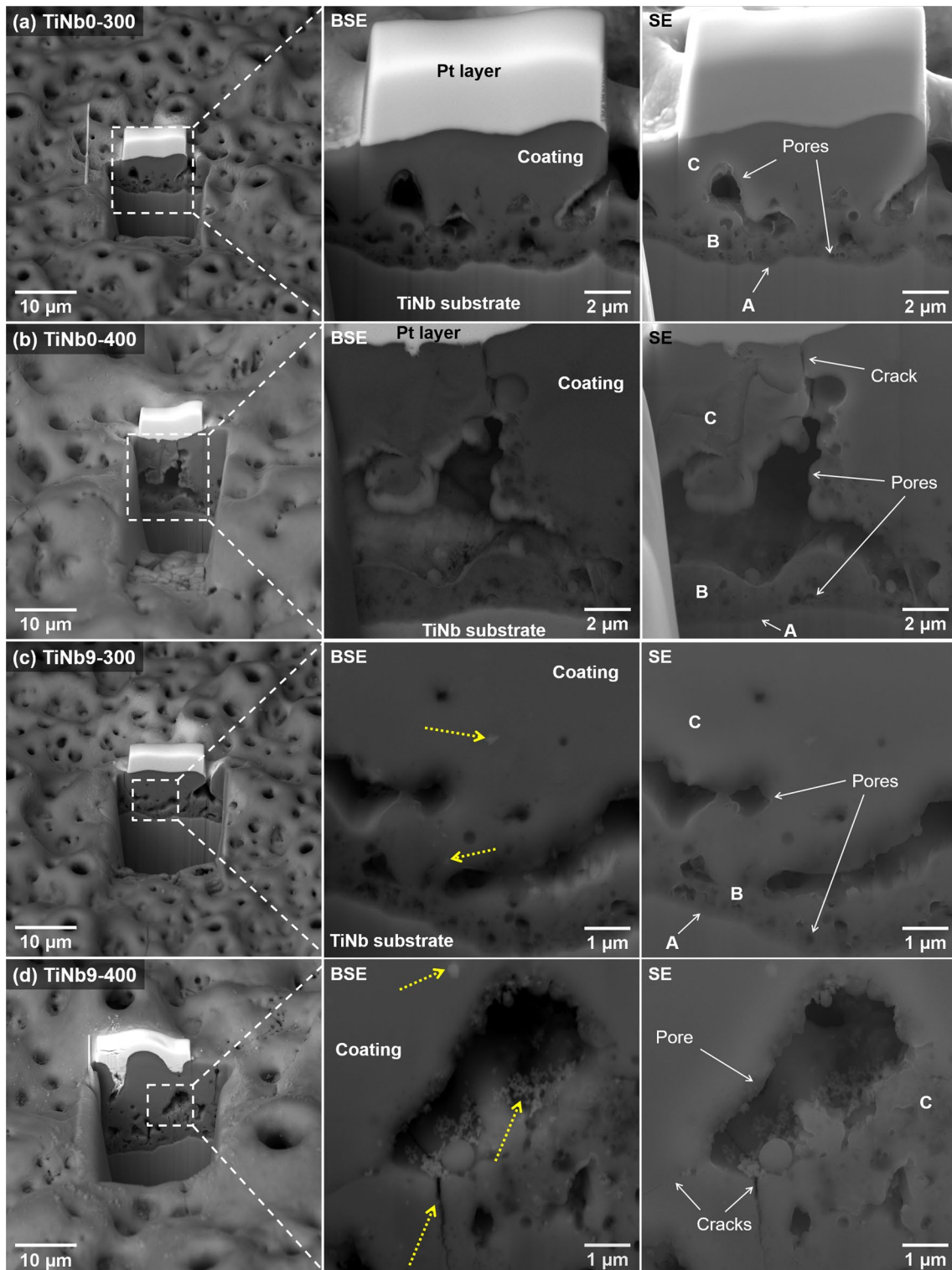
Fig. 5 Cross-sectional FIB-SEM micrographs of the **a** TiNb0-300, **b** TiNb0-400, **c** TiNb9-300, and **d** TiNb9-400 coatings, with their respective higher magnification selected zones in both backscattered electron (BSE) and secondary electron (SE) modes. ZrO$_2$ NPs indicated by dotted arrows

Fig. 6 XRD patterns of the as-functionalized samples, and reference to Rutile/Anatase (R/A) and ZrO_2/TiO_2 ratios
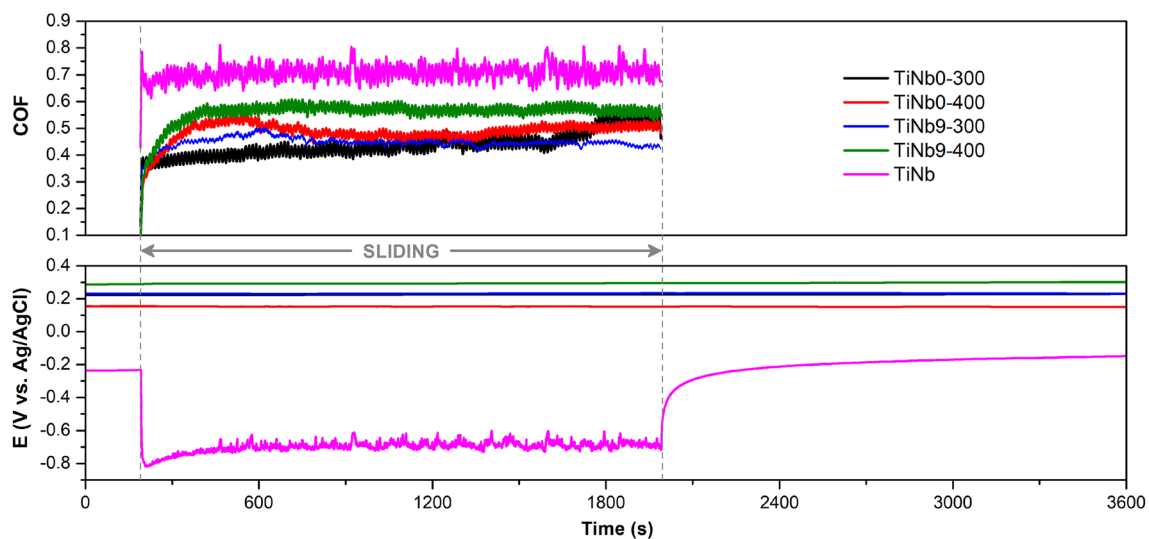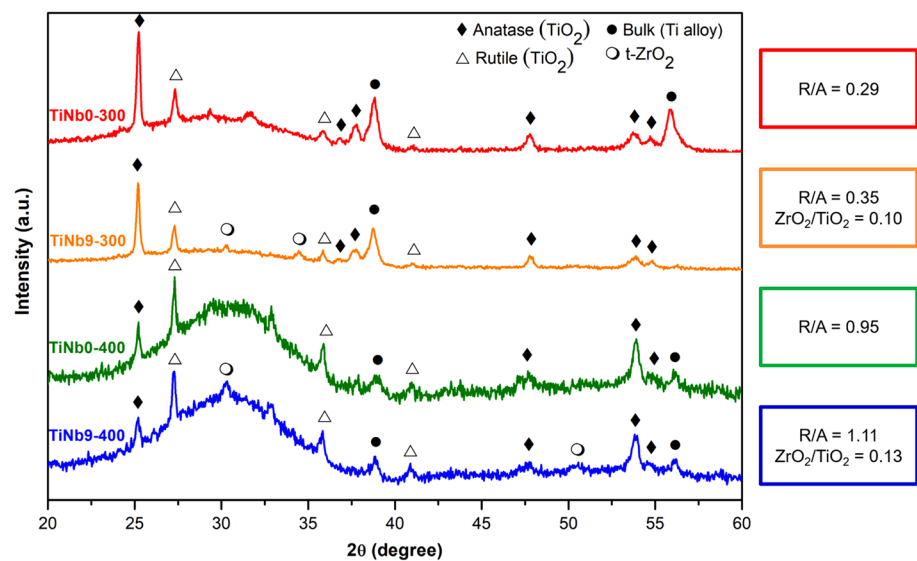

Fig. 7 Representative OCP and COF evolution recorded during tribocorrosion tests in PBS under 2 N normal load for TiNb, TiNb0-300, TiNb0-400, TiNb9-300, and TiNb9-400 samples

anodic films. In fact, those variations were too small to be detected in the meantime on the OCP evolution.

Figure 8 gives representative lower magnification SEM images of the wear tracks, taken in backscattered electron (BSE) and secondary electron (SE) modes. Darker areas on BSE mode can be related to oxidized regions for both bare alloy and coated samples, whereas the most damaged areas of the coatings can be identified by brighter zones. Untreated TiNb samples (Fig. 8a) exhibited typical worn surface features for Ti, indicating abrasive wear as highlighted by parallel sliding grooves, together with some compacted oxidized wear debris [10, 57].

The wear tracks of all MAO-treated groups (Fig. 8b–e) presented poor exposure of the substrate (brighter zones), confirming the stable OCP evolution. Considering the groups treated at 300 V (Fig. 8b, d), similar wear tracks can be observed regardless of the presence of ZrO_2 NPs. The top peaks of the coating were erased, producing wear debris that eventually filled up and covered undamaged porous structures, finally creating smoothed zones as the alumina ball moved [27]. However, the worn surface appears to be affected when the potential was increased to 400 V. Indeed, the samples treated without nanoparticles (Fig. 8c) presented wear scar dimension significantly higher comparing to the
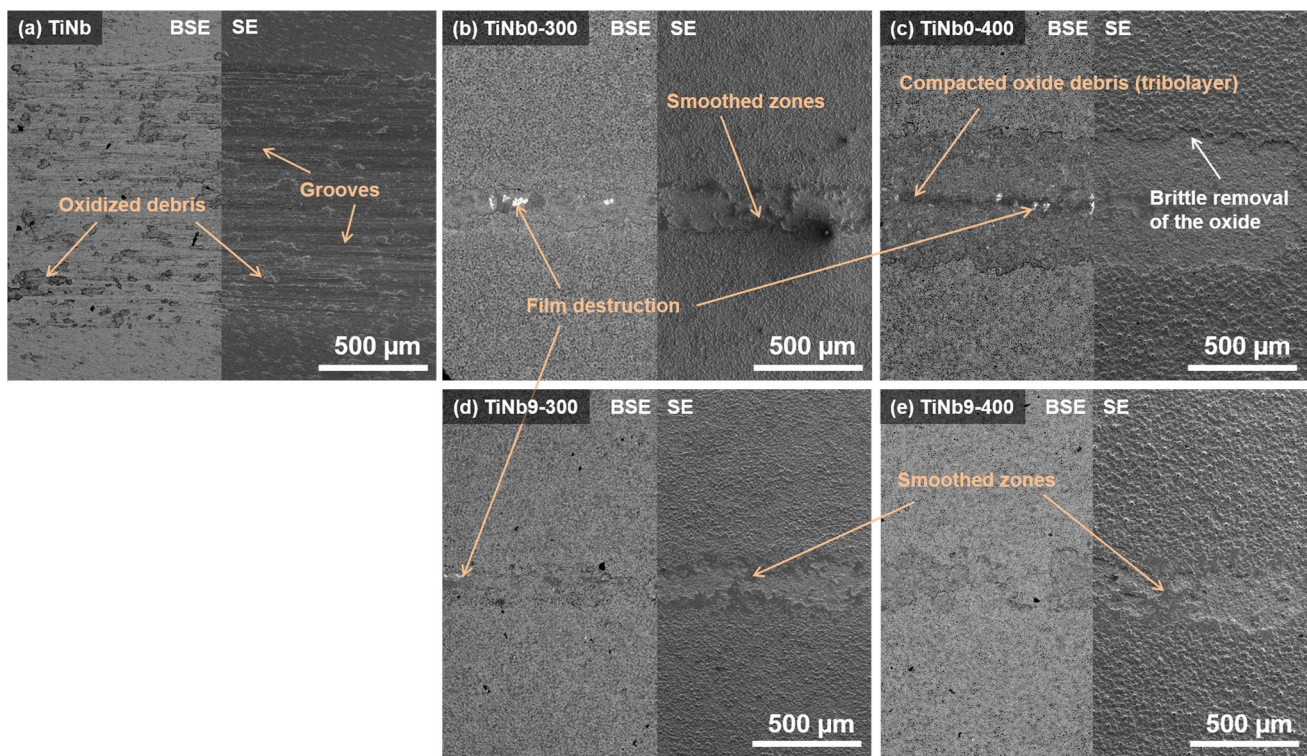
Fig. 8 Lower magnification SEM images of the worn **a** TiNb, **b** TiNb0-300, **c** TiNb0-400, **d** TiNb9-300, and **e** TiNb9-400 samples, after tribo-corrosion tests under 2 N

other anodic films, although still smaller than the one of the TiNb samples. In the periphery of the wear track, it is also observed an evident brittle removal of the outermost oxide layer. Some of the resulting oxide debris from these regions may have contributed to form a tribolayer in central zones of the wear track, as consequence of smashing and compaction in the contact region. On the other hand, these features could not be observed when the samples were treated with ZrO_2 NPs (Fig. 8e). In fact, for those tribocorrosion experiments under 2 N loading, TiNb9-400 samples presented worn surface features similar to the ones observed on the TiNb0-300 and TiNb9-300 samples. Figure 9 shows a more detailed view on the wear tracks of the MAO-treated coatings, confirming different worn surfaces between TiNb0-400 and the other as-functionalized samples.

3.2.2 Normal Load: 3 N

The MAO-treated coatings were also tested under more severe conditions (3 N loading), and the evolution of both OCP and COF during these new experiments is shown on Fig. 10. By applying higher contact pressures, the OCP evolution obtained during sliding was clearly affected. Both TiNb0-300 and TiNb9-300 coatings presented a sudden drop on OCP after some period of sliding, followed by a small decreasing trend. This behavior may be related to a severe

damage of the anodic film in multiple regions over the wear track, as result of the harsher rubbing of the oxide layers against counter material at higher contact pressures. Then, the wear debris created can be smashed through the continuous movement of the alumina ball, resulting in the formation of a tribolayer (as it will be exhibited ahead) that may give a limited protective role, retarding further sharp decays on OCP [10, 59]. The OCP falls down early for the TiNb9-300 surfaces; however, this decrease was relatively slow and the OCP values remained slightly nobler as compared to the TiNb0-300 groups during sliding.

Concerning the OCP evolution on the TiNb0-400 samples, it can be observed smaller OCP decay in comparison with the MAO surfaces treated at 300 V. This slow decreasing trend was interrupted when the counter-body stopped moving. In contrast, when ZrO_2 NPs were added, the OCP evolution kept unaltered throughout the test for the TiNb9-400 samples.

The OCP evolution is interconnected to the COF values, as it can be also seen on Fig. 10. As general, significative increases on COF values were accompanied by significative drops on OCP, as mostly evidenced for the TiNb0-300 and TiNb9-300 groups that may suggest the appearance of some large regions of the substrate after film destruction.

Figure 11 presents the wear tracks of the MAO-treated coatings after the tests under 3 N loading, taken on both
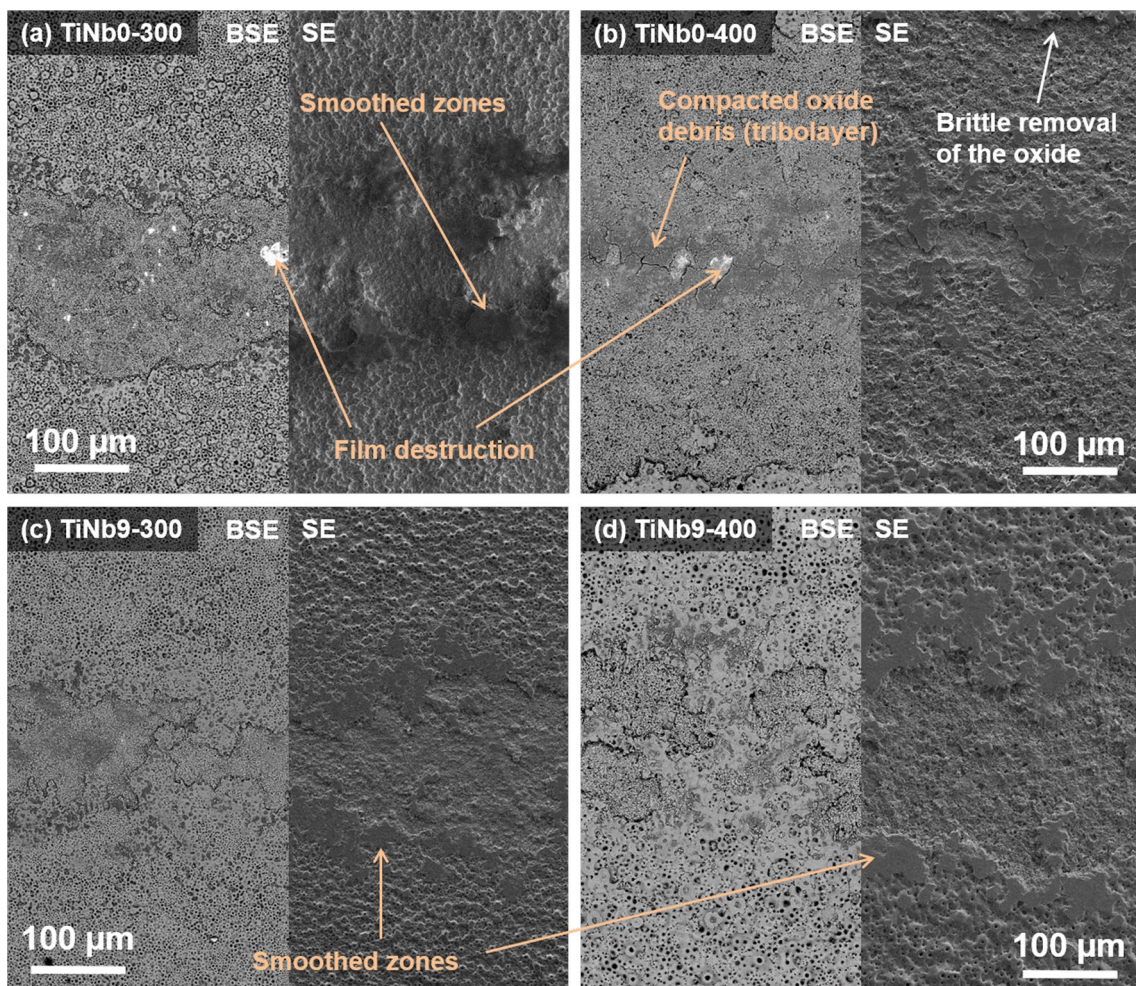
Fig. 9 Higher magnification SEM images of the worn **a** TiNb0-300, **b** TiNb0-400, **c** TiNb9-300, and **d** TiNb9-400 samples, after tribocorrosion tests under 2 N

Fig. 10 Representative OCP and COF evolution recorded during tribocorrosion tests in PBS under 3 N normal load for TiNb0-300, TiNb0-400, TiNb9-300, and TiNb9-400 coatings

Fig. 11 Lower magnification SEM images of the worn **a** TiNb0-300, **b** TiNb0-400, **c** TiNb9-300, and **d** TiNb9-400 samples, after tribocorrosion tests under 3 N
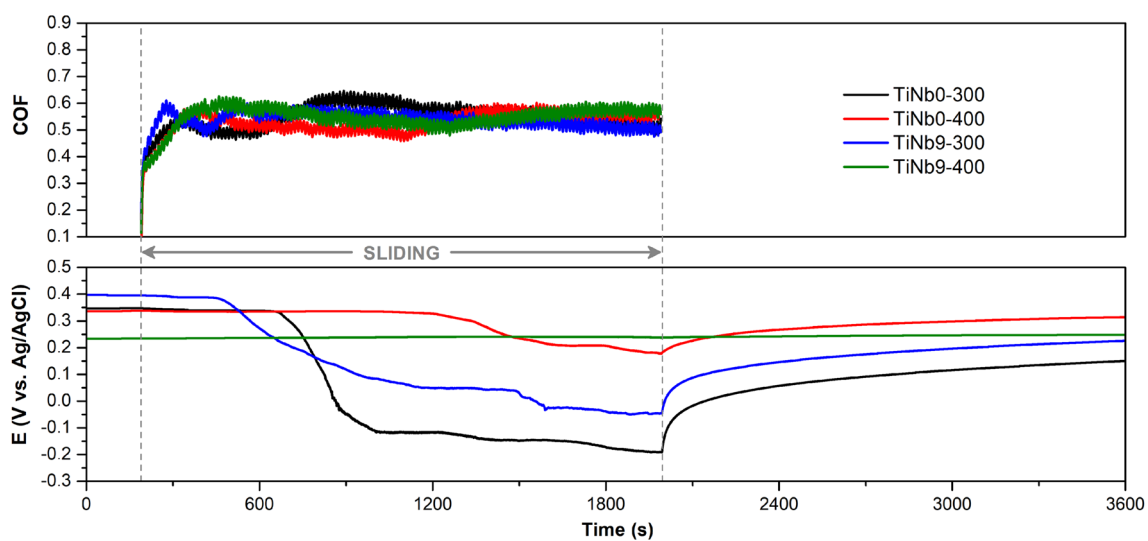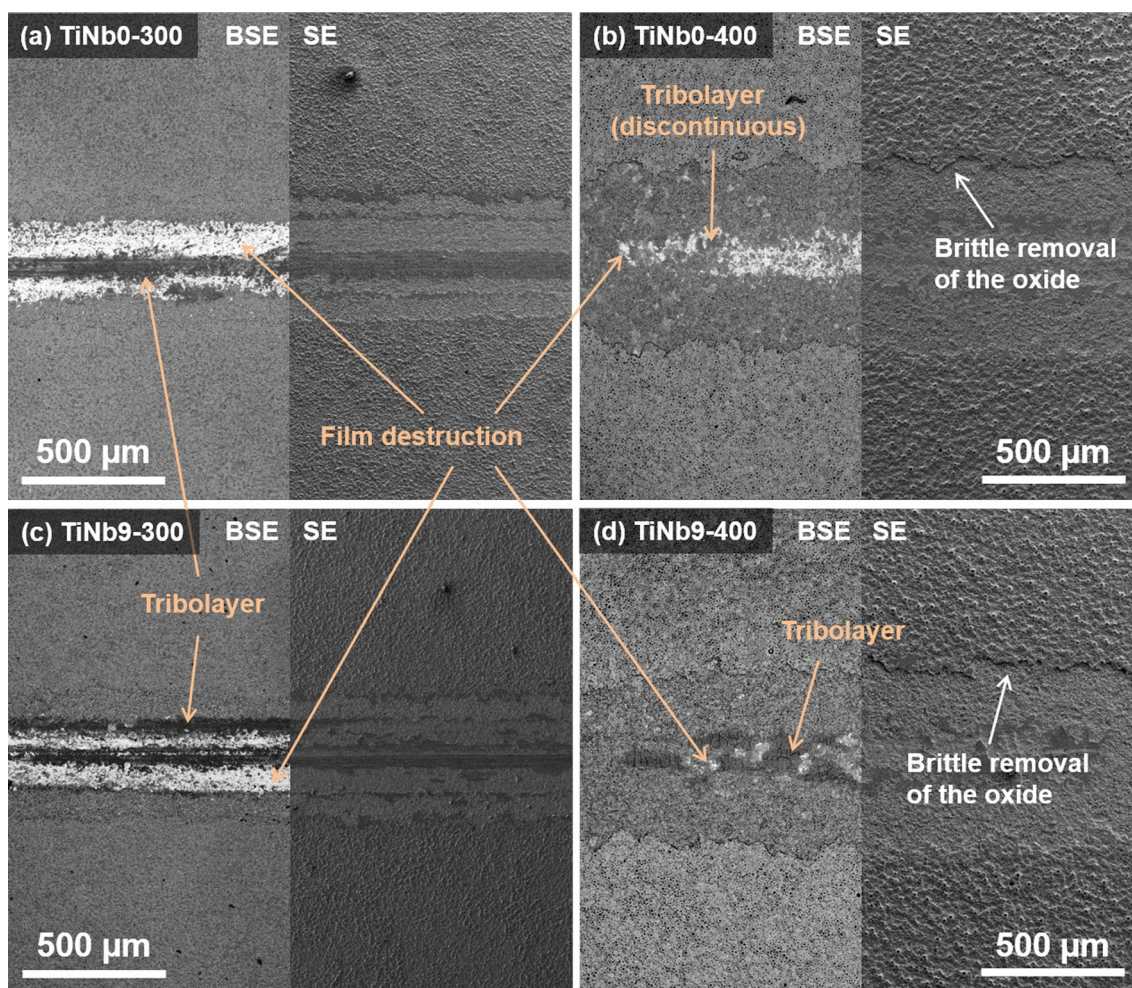
BSE and SE modes in lower magnification. As general, the 300 V-treated groups showed very similar wear tracks (Fig. 11a, c), with huge areas of film destruction, as well as an evident tribolayer represented in the central region of the wear track. However, some of the oxide layers maintained their integrity in the periphery of the contact region with alumina ball. Moreover, it seems that the TiNb9-300 coatings presented some more oxidized zones over the central region of the wear track as compared to the TiNb0-300 samples, which may be associated with the slightly nobler OCP values on the TiNb9-300 samples, retarding higher exposure of the underlying TiNb substrate to the corrosive effect of PBS.

When the 400 V-treated samples were tested under higher loading conditions (3 N), their outermost oxide layers could not withstand, resulting in an expanded wear track characterized by brittle oxide removal in its periphery, as observed on the Fig. 11b, d. However, a much less exposure of the substrate (brighter zones in BSE mode) is also observed on

the wear tracks, comparing the ones of the 300 V-treated groups. The differences in the wear tracks between TiNb0-400 and TiNb9-400 samples seem to be mostly attributed to the visible mechanical damage. The wear of the TiNb0-400 samples appears to be at a higher stage of development, as more regions of film destruction could be detected on the wear scar. Besides, TiNb9-400 samples showed a tribolayer in the central region of the wear track, whereas TiNb0-400 samples presented a few adhered patches representing a discontinuous tribolayer, which may provide a very limited protection [57].

Figure 12 exhibits a closer look at the worn surfaces after mechanical solicitations carried out under 3 N normal load, along with EDS spectra obtained from the characteristic zones. Three typical distinguished zones can be detected in the wear tracks. Zones where the substrate was exposed after film destruction (Z1, Z4, and Z7), which are represented by higher amount of Ti and Nb (substrate), lower concentration of O, and poor quantity of bioactive elements (Ca, P, Mg,
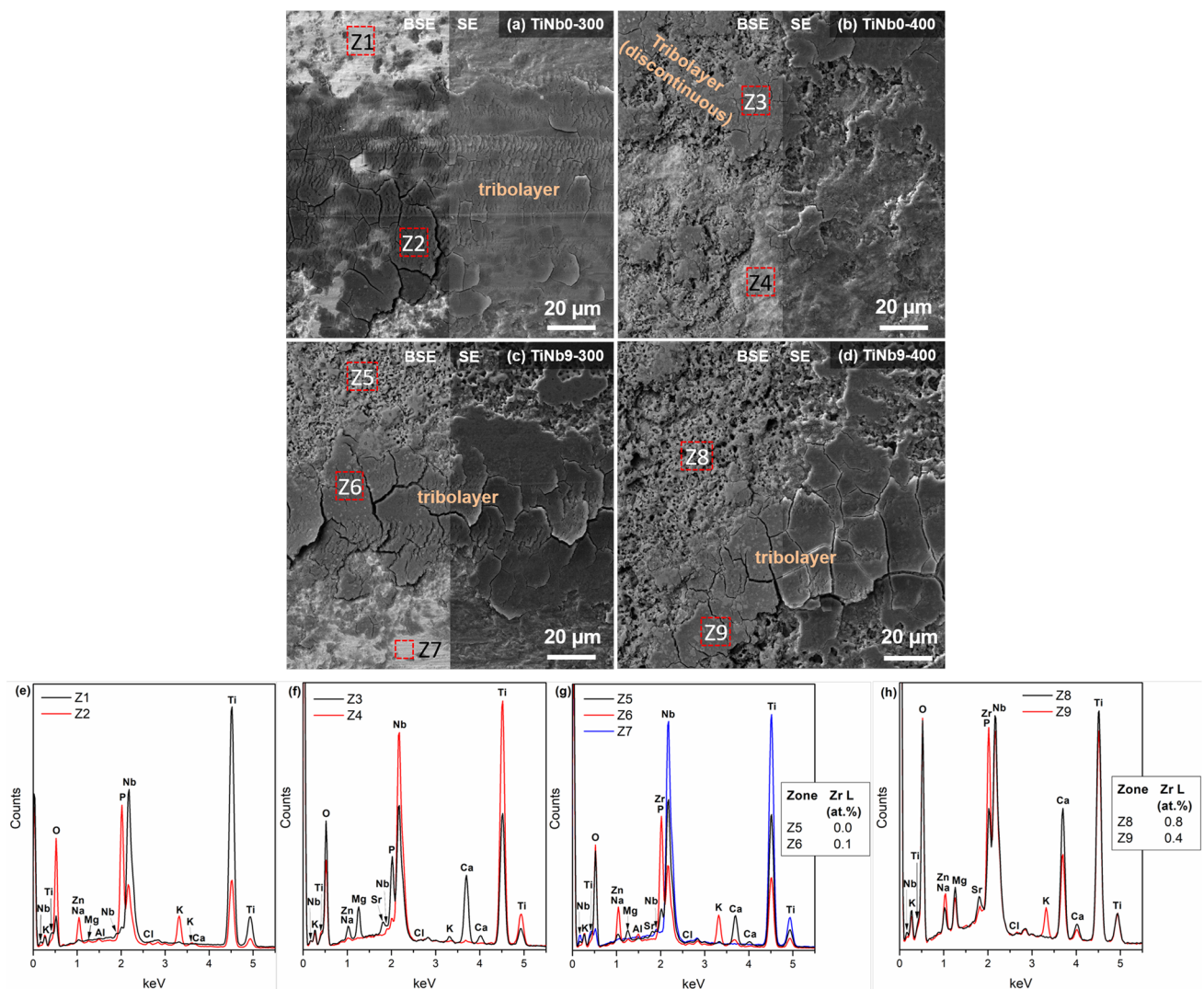
Fig. 12 Higher magnification SEM images of the worn **a** TiNb0-300, **b** TiNb0-400, **c** TiNb9-300, and **d** TiNb9-400 samples, together with correspondent **e–h** EDS spectra taken from the inset red zones (Z1– Z9), after tribocorrosion tests under 3 N. Atomic percentage (at.%) of the element Zr L inserted on (**g**) and (**h**)

Zn, and Sr). Part of these removed anodic layers (mixture of titanium and niobium oxides) was re-deposited to the surface through continuous compaction during sliding, forming a tribolayer (zones Z2, Z3, Z6, and Z9) rich in bioactive agents, together with high amount of elements from the physiological fluid, such as K, P, Na, and Cl. Other oxidized zones represent the surface practically not disturbed (Z5 and Z8), maintaining its porous morphology, and incorporated with the bioactive elements through the anodic treatment, with low presence from PBS composition.

TiNb0-300 surfaces (Fig. 12a) mainly exhibited two distinctive zones; Z1 represents film destruction, whereas Z2 depicts a tribolayer, due to the large difference on the O, Ti, and Nb contents (Fig. 12e). An additional oxidized zone (Z5) is observed on the wear track of the TiNb9-300

samples (Fig. 12c), not significantly damaged and still biofunctionalized (Fig. 12g). Traces of the element Al may indicate transfer of material from the counter-body to both coatings grown at 300 V. A discontinuous tribolayer (Z3) is verified on the TiNb0-400 samples (Fig. 12b), along with a zone of film destruction (Z4) characterized by a significant increase of Ti and Nb and practically no content of bioactive species (Fig. 12f). The wear track of the TiNb9-400 samples can be observed in more detail on Fig. 12d (the few and small areas of film destruction—represented by brighter areas (BSE mode) on Fig. 11d—were not analyzed). There is a huge presence of O and bioactive agents in both zones Z8 and Z9 (Fig. 12h). Element Zr could be well detected in these regions, instead of the zones Z5 and Z6 on TiNb9-300 surfaces.

Figure 13 shows FIB prepared cross-sectional SEM images of the worn sub-surfaces, taken as perpendicular to the sliding direction after tribocorrosion tests under 3 N normal loading. The coating grown during MAO treatment on the TiNb0-300 surfaces (Fig. 13a) was not observed under the tribolayer formed. Instead, it was identified a severe damage to the metallic substrate, characterized by a plastic deformation. Concerning both TiNb0-400 and TiNb9-300 samples (Fig. 13b, c, respectively), the porous coating was still found under tribolayer, but presenting a significant damage characterized by either extensive propagation of cracks previously formed during MAO, or nucleation of new ones that possibly were induced by mechanical actions. This type of damage seems to be even more aggravated for the TiNb0-400 coatings, which also presented some cracks near the metal/oxide interface. In contrast, TiNb9-400 coatings showed sub-surface cracks at a lower level of development (Fig. 13d). For these samples, some wear debris were found deposited inside the pores. As it was analyzed before tribocorrosion experiments (on the Fig. 5c, d), ZrO_2 NPs (indicated by dotted arrows) were preferentially identified along the oxide layers of the TiNb9-400 samples (either inside the pores and cracks, or embedded in the coating), in comparison with the TiNb9-300 samples which mostly presented some embedded nanoparticles.

4 Discussion

This work aimed at studying, for the first time, the tribocorrosion behavior of bio-functionalized ZrO_2 nanoparticles-containing MAO coatings grown on Ti-40Nb alloy. The following subsections emphasize important topics, such as growth mechanisms of the MAO coatings, incorporation of ZrO_2 NPs, and the tribocorrosion behavior of the novel surfaces developed.

4.1 General Growth Mechanisms of the MAO-Treated Coatings

Ti-40Nb substrates were coated by micro-arc oxidation in the report of Gebert et al. [36]. As general, the alloy followed the same oxide growth mechanisms established for titanium. In this light, it is believed that all coatings in the present work were formed through the same main stages reported for bulk Ti treated by similar MAO parameters [23, 27, 30, 56, 60]. During the initial moments of the process, the metallic substrate goes through a uniform film growth stage, which is linked to the formation of a compact and thin oxide layer, generally called by barrier film [23, 56] as depicted in Fig. 5. Afterwards, by reaching a critical potential value, a phenomenon named dielectric breakdown takes place at sites of the oxide with less resistance, originating

numerous energetic micro-arcs (sparks) and discharges over the surface. After the appearance of such features, a cascade of events has been discussed. The high temperatures and pressures promoted by the micro-arcs, contribute to the formation of small nanocrystals such as anatase and rutile into the amorphous matrix of the coating [27, 30] (as seen by the XRD analysis on Fig. 6). Due to its higher ionic resistivity comparing to the one of amorphous phase, the crystalline oxide can favor the oxygen (gas) generation within the coating [61, 62]. Formation of pores is also a typical consequence of the high local temperatures achieved by the micro-arcs spread over the entire surface, as well as of the eventual bursting of some oxygen-filled bubbles occluded in the growing anodic film. Meanwhile, in the process of local melting and fast re-solidification of the oxide in contact with the electrolyte, the bioactive elements from the electrolyte are allowed to be incorporated into the new coating material [27, 30], as it was observed the successful incorporation of Ca, P, Mg, Zn, and Sr species by EDS analysis (Fig. 4). It is noteworthy that the presence of Nb detected by chemical mapping may indicate that all coatings were also composed of niobium oxide such as amorphous Nb_2O_5 [62]. Sparks are continually initiated and extinguished at spots of dielectric breakdown as the new local coating material restores the resistance to the current flow [63]. As potential is increased with time, the micro-arcs and discharges become more powerful, leading to the formation of larger and protruding pores [27]. As final result, it is observed a multi-scale porous surface (Fig. 3) and a cross-section with triplex structure (barrier film, inner porous layer, and outer porous layer) (Fig. 5), according to the results of Alves et al. [23, 56] for Ti coated by similar MAO parameters. Furthermore, both porous layers are thicker than the barrier film as the current flow concentrates at the sparking locations, contributing for a faster and localized thickening of the oxide [63].

When the MAO treatments were performed by applying a higher voltage (400 V), some specific characteristics of the coatings were affected. It is reported that the voltage of anodization has a significant effect on the intensity of the sparks formed during the oxide growth [64, 65] and, as previously discussed, various properties of the MAO coatings are strongly dependent on the sparking events occurring at the surface. The higher potential applied could have contributed for micro-arcs and discharges more energetic, leading to higher local temperatures and pressures and facilitating the transformation of anatase to rutile [56], which is evidenced by higher R/A ratio as in the case of the 400 V-treated groups of this work (Fig. 6). By using similar processing parameters of this study, Oliveira et al. [27] explained that the outermost parts of the anodic film are expected to re-solidify at first so quickly that an atomic rearrangement could not take place, what ends up in coatings containing an amorphous layer at superficial regions. This
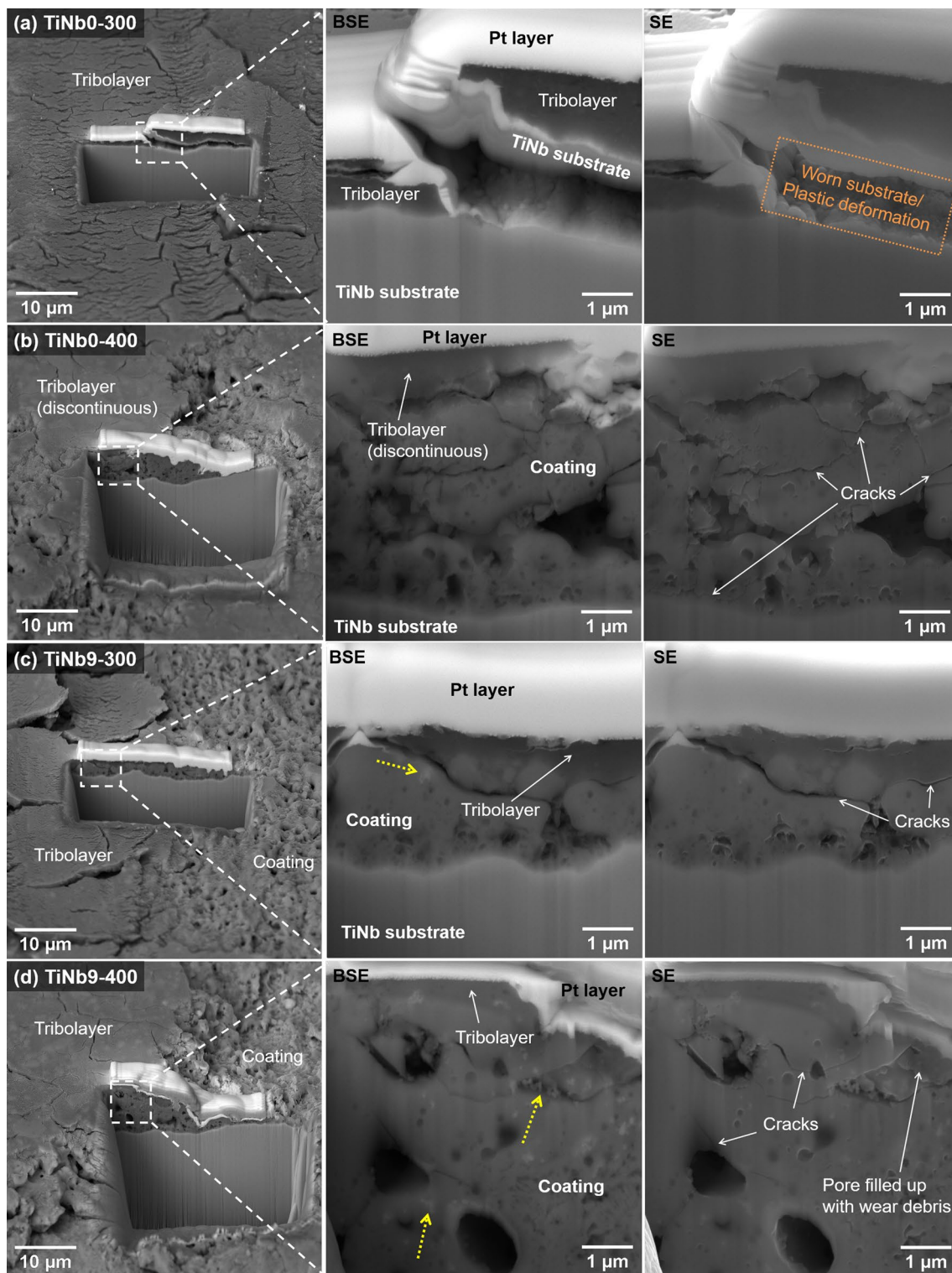
Fig. 13 Cross-sectional FIB-SEM micrographs taken from wear tracks of the **a** TiNb0-300, **b** TiNb0-400, **c** TiNb9-300, and **d** TiNb9-400 samples after tribocorrosion tests under 3 N, with their respective higher magnification selected zones in both backscattered electron (BSE) and secondary electron (SE) modes. ZrO_2 NPs indicated by dotted arrows

finding was also reported by Ribeiro et al. [30]. The characteristic shoulder of amorphous phase found on XRD analysis (Fig. 6) may suggest that the 400 V-treated groups presented an increased amorphous content at the superficial regions, although further investigation needs to be conducted in order to confirm this assumption. The appearance of cracks has been presumed from thermal stresses due to the sharp drop in the temperature of the molten oxide in contact with cold electrolyte, and/or stresses due to phase transformations in the coatings [66], which were both conditions more prone to occur for the potential applied of 400 V. Therefore, cracking phenomenon was more clearly observed on the surface (Fig. 3b, d) and along the cross-sections (Fig. 5b, d) of the 400 V-treated samples. In addition, cracks are among the zones more prone to dielectric breakdown [27], which may have originated several crack-liked tracks accompanied by small pores over the surface (Fig. 3b, d). These features may have significantly contributed for smaller surface porosities for the 400 V-treated groups, despite the presence of some larger and elongated pores due to the more powerful micro-arcs. TiNb0-400 and TiNb9-400 coatings were significantly thicker thanks also to the micro-arcs and discharges more energetic [65]. Finally, MAO processing at higher voltage did not affect the successful incorporation of the bioactive species (Ca, P, Mg, Zn, and Sr), which were uniformly distributed over the surface as observed in representative EDS mapping (Fig. 4).

4.2 Incorporation of ZrO$_2$ NPs into the MAO-Treated Coatings

It has been reported that most of the particles are negatively charged in alkaline electrolytes by acquiring a negative surface charge [37], as observed for ZrO$_2$ NPs in several works [40, 43, 50, 51, 67]. Afterwards, through electrophoresis, the charged ZrO$_2$ NPs suspended in the electrolyte can migrate towards the anode under influence of the electric field. The electrophoretic velocity (v) of the nanoparticle suspension is given by Eq. 2:

$$v = \frac{QE}{4\pi r \eta} \tag{2}$$

where Q is the surface charge of the particles, E is the potential difference applied to the particle suspension to generate the electric field, r is the particle radius, and η is the viscosity of the particle suspension [68]. As the composition of the base electrolyte and the type, size, and concentration of nanoparticles were the same for both TiNb9-300 and TiNb9-400 samples, the parameters Q, r and η can be considered constant. Therefore, the voltage of the MAO treatment was the principal factor affecting the electrophoretic velocity of the ZrO$_2$ NPs. This indicates that MAO treatments at 400 V

facilitate the incorporation of nanoparticles, making them move more easily towards the positive electrode (TiNb substrates) under effect of the higher electric field.

Micro-arcs and discharges also play a key role on the incorporation of nanoparticles, creating opportunities for them to either be inertly incorporated or be incorporated by chemical reactions. In the first possibility, the particles are generally introduced to the coatings through different transport pathways (e.g., open pores, cracks, and short-circuit channels) without forming new phases; consequently, they are easily traced and identified in the oxide layers by imaging techniques, even if some superficial chemical reaction may take place at the particle/coating interface [37, 46, 69]. In the second case, the particles can be entirely melted due to the high local temperatures achieved, and then react with other components from electrolyte and coating matrix, originating new zirconium compounds such as ZrTiO$_4$ [38, 51].

In this work, the main locations of ZrO$_2$ NPs (which were observed embedded or protruded from the oxide, and also inside the pores and cracks) are clearly distinguishable as brighter regions due the atomic number contrast on BSE mode (Figs. 3c, d, 5c, d), which are supported by EDS analysis (Fig. 4b). Interestingly, with regard of the cross-sections, the nanoparticles were only identified above the barrier film (Fig. 5c, d), which confirms the essential role of powerful micro-arcs and discharges on the incorporation of ZrO$_2$ NPs. Moreover, there was no formation of new compounds, as only tetragonal-phase peaks of the original ZrO$_2$ NPs were found for both TiNb9-300 and TiNb9-400 samples (Fig. 6). Therefore, it can be assumed that the ZrO$_2$ NPs were inertly incorporated into the MAO-treated coatings, even after sparking events more energetic taking place on the TiNb9-400 surfaces due to the higher voltage applied. Inert incorporation of zirconia nanoparticles is also demonstrated by other studies [39, 40, 45, 46].

The addition of nanoparticles did not affect the success of the incorporation of bioactive elements (Ca, P, Mg, Zn, and Sr), which could be analyzed in both TiNb9-300 and TiNb9-400 coatings (Fig. 4b). An in-depth quantitative chemical analysis of these elements and their impact on biological properties are in the scope of further investigation. On the other hand, some modifications on the thickness, R/A ratio, and surface porosity could be observed for the ZrO$_2$ NPs-treated coatings (especially in the case of the TiNb9-400 samples) as compared to the nanoparticle-free ones. Similar observations are already reported in the literature [43, 67]. It has been explained that the presence of nanoparticles in the electrolyte can contribute to the oxide growth due to the higher consumption of the plasma energy at sparking sites [51]. That higher energy consumption may also have contributed to the transformation of anatase to rutile, which was highlighted by higher R/A values for the samples containing nanoparticles (Fig. 6), especially for the TiNb9-400 coatings

that were produced under conditions of better migration of ZrO_2 NPs towards the oxide/electrolyte interface. On the other side, the surface porosity can be decreased as nanoparticles agglomerate inside the pores, creating a sealing effect [67, 70], which probably was more evident for the TiNb9-400 samples as also consequence of the higher electrophoretic attraction.

In fact, in direct comparison between TiNb9-300 and TiNb9-400 coatings, some differences can be found regarding the incorporation of ZrO_2 NPs. Such particles are not so visible throughout the cross-section of the TiNb9-300 samples, as opposite for the TiNb9-400 coatings which presented abundant nanoparticles inside the pores and cracks as well as embedded in the oxide (Fig. 5c, d). Together with higher values of crystalline ZrO_2/TiO_2 ratio (Fig. 6), these results suggest preferential incorporation of nanoparticles for the TiNb9-400 samples, as result of combined effect of better delivery of ZrO_2 NPs and stronger micro-arcs and discharges during MAO processing at higher voltages [44].

To sum up, the mechanism of ZrO_2 NPs incorporation is proposed by four main stages as shown on Fig. 14. The nanoparticles get negative surface charge when suspended in alkaline electrolyte (Fig. 14a). By applying a potential difference between electrodes, the nanoparticles start to be attracted to the surroundings of the anode by electrophoresis (initial stages of the anodic process corresponding to the formation of a barrier film) (Fig. 14b). After dielectric breakdown, the high local temperatures caused by micro-arcs and discharges lead to a physical mixing between attracted ZrO_2 NPs and the fluctuating molten titanium oxide, along with some superficial chemical mixing that may take place at their interfacial region (Fig. 14c). Once the sparking events extinguish and the zones are cooled by the electrolyte, ZrO_2 NPs become entrapped at the sites of oxide growth, being found inside the pores or cracks, or embedded in the coating (Fig. 14d). Moreover, some nanoparticles can be observed protruding from the surface, as a result of deposition or possible superficial chemical mixing to the oxide.

4.3 Tribocorrosion Behavior of Bio-Functionalized ZrO_2 NPs-Containing MAO Coatings

Ponthiaux et al. [71] have explained that the OCP provides important information on the electrochemical state of the material. A more passive state is reflected by an increase in the OCP (anodic shift); as opposite, a more active state is given by a decrease (cathodic shift). All as-functionalized samples showed undoubtedly better tribo-electrochemical response than the untreated TiNb substrates in the tests under 2 N loading (Fig. 7). The MAO layers provided protection for the surfaces, avoiding exposure of the underlying substrate (Figs. 8, 9). In fact, the porous structures can act as entrance channels for corrosive fluids. However, MAO-treated coatings grown by similar parameters of this work
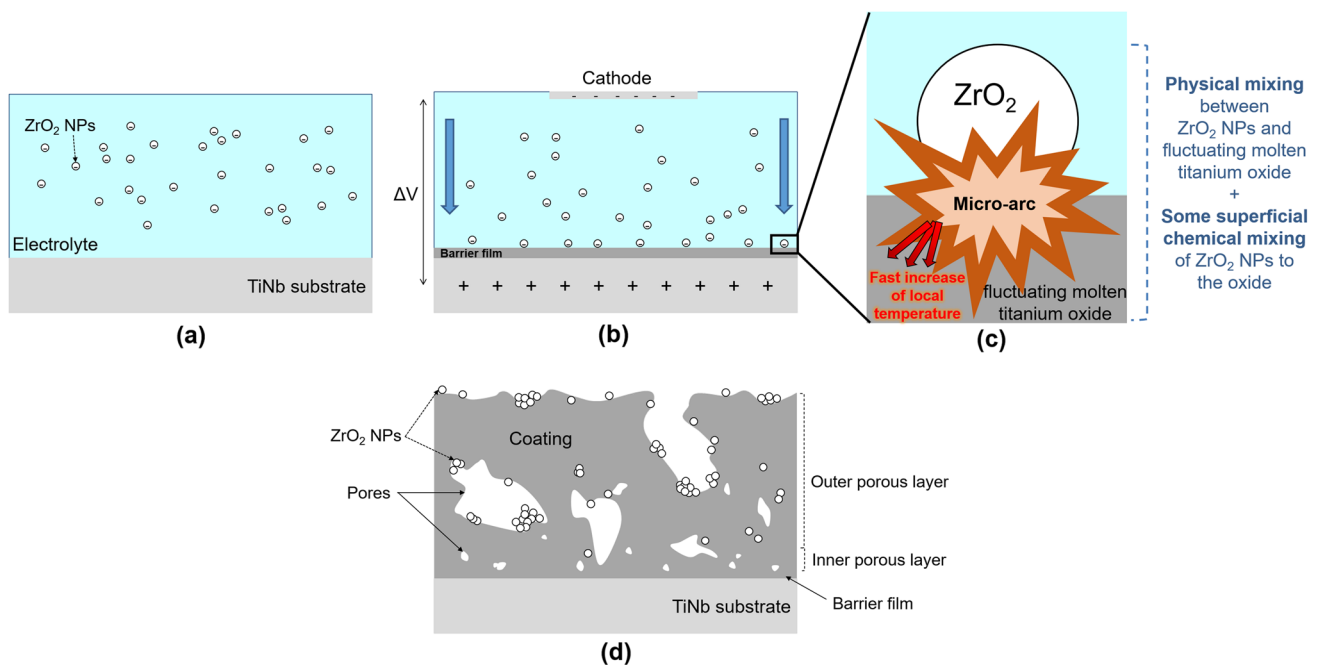

Fig. 14 Schematic illustration of the suggested incorporation mechanism of ZrO_2 NPs, divided into four main stages: **a** negative surface charged nanoparticles in alkaline electrolyte, **b** attraction of the nanoparticles to the anode by electrophoresis, **c** physical mixing (along with some superficial chemical mixing) between nanoparticles and fluctuating molten titanium oxide caused by sparking events, and **d** entrapment and preservation of nanoparticles at the sites of oxide growth and coating surface

have improved the corrosion behavior of the material, mostly due to the presence of the barrier film [23, 56, 60]. On the other side, higher asperities of those MAO surfaces suffer from the greatest contact pressures under loading conditions, becoming more prone to mechanical degradation [27]. Nevertheless, tiny wear debris can be accumulated in the lower zones and undamaged pores, creating smoothed zones and minimizing the chances of wear by third-body abrasion, which is commonly reported for contacts between flat surfaces, being very detrimental for the material [10]. As explained by Oliveira et al. [27], the increased tribocorrosion resistance of MAO coatings can also be due to the mixture of anatase and rutile, with preferential presence of rutile around the upper pores, acting as an effective barrier against severe deterioration.

However, it is important to pay attention to the quantity of rutile formed. While the presence of rutile can improve mechanical properties of the MAO-treated coatings [25, 27, 72], it is also expected that, after some period under high loading conditions, these materials can be more prone to brittle cracking associated with the harder rutile [27]. TiNb0-400 samples may have severely suffered from this phenomenon as evidenced by the morphology of destruction of their anodic film (Figs. 8c, 9b). That brittle oxide removal in the peripheral regions of the wear track can be quite undesirable, since it can give rise to large third-body particles, which can freely move on the surface aggravating even more the damage [10, 27], or be released to the host environment and compromise biological functions. This quantity of visible damage could not be identified when the samples were treated with ZrO_2 NPs (TiNb9-400 groups) (Figs. 8e, 9d), which might indicate a delayed effect on the brittle removal of the outermost oxide layers. This assumption is further confirmed when the MAO-treated coatings were also tested under more severe conditions (3 N as normal load).

By applying higher contact pressures, the OCP evolution obtained during sliding reflected more clearly the mixed potential values, from both active (worn) and passive (unworn) zones in the wear track. Also, the characterization of both wear tracks and the worn sub-surfaces could provide valuable information on the wear mechanisms. It is reasonable to state that the processing voltages together with the incorporation of ZrO_2 NPs played a key role on the resulting wear mechanisms of the coatings.

The 400 V-treated groups did not share the same wear mechanisms of the coatings submitted to 300 V. Tribolayers on the TiNb0-300 (Fig. 12a, e) and TiNb9-300 (Fig. 12c, g) samples, presented some Al that may indicate the transfer of material from the alumina ball during sliding. Even under higher loading conditions (3 N), both TiNb0-400 and TiNb9-400 surfaces presented much less visible mechanical damage (exposure of the substrate) (Fig. 11b, d) comparing to the 300 V-treated groups (Fig. 11a, c). However, the

favorable formation of rutile seems to induce brittle removal of the outermost oxide layers, as it is clearly observed an enlargement of the wear tracks for the 400 V-treated groups. These findings reinforce that both TiNb0-400 and TiNb9-400 coatings presented similar wear mechanisms (but different from the 300 V-treated groups), although the incorporation of ZrO_2 NPs could provide some more protection to the superficial oxide layers as also observed during the previous test (2 N loading), minimizing in that case a brittle oxide removal (Fig. 8c, e).

It is suggested that an enhanced inert incorporation of ZrO_2 NPs could better accommodate the internal stresses and retard the eventual phenomena of brittleness and cracking associated with rutile during vigorous mechanical solicitations. In fact, possible damage owing to fatigue wear appears to occur at a lower stage of development for the TiNb9-400 samples (Fig. 13d), in contrast to the extensive nucleation and/or propagation of sub-surface cracks for the TiNb9-300 (Fig. 13c) and TiNb0-400 (Fig. 13b) groups.

To sum up, the Fig. 15 shows schematically the wear mechanisms proposed for the as-functionalized samples tested in this work. TiNb0-300 samples (Fig. 15a) showed mainly joint features of abrasive and adhesive wear, which were evidenced by various zones of complete film destruction, reaching the substrate and provoking plastic deformation, as well, the formation of tribolayers (with some transfer of Al from counter material). The visible surface damage was slightly reduced for the TiNb9-300 samples (Fig. 15b), but they may also have presented signs of fatigue wear governed by sub-surface cracks in the MAO layers. When the coatings were grown at higher processing voltages, zones of exposure of the substrate were significantly reduced, and the coatings seem to be mostly damaged in the top oxide layers (Fig. 15c, d). However, TiNb0-400 samples exhibited more zones of film destruction as compared to TiNb9-400 samples. Without nanoparticles, the coatings were covered by some small oxidized patches (discontinuous tribolayers) offering a very limited protection, and an extensive nucleation and/or propagation of cracks was detected throughout the remaining oxide layers (Fig. 15c). On the other hand, an enhanced inert incorporation of ZrO_2 NPs (TiNb9-400 coatings, Fig. 15d) may have delayed eventual phenomena of brittleness and cracking associated with harder materials (rutile) under vigorous mechanical solicitations.

4.4 Limitations of the Present Study

In this paper, a first insight on the tribocorrosion behavior of micro-arc oxidation films incorporating ZrO_2 particles was investigated. Due to the novelty of the study, it was decided to report the obtained results that open new directions for further research. Therefore, limitations of the present work should be referred.
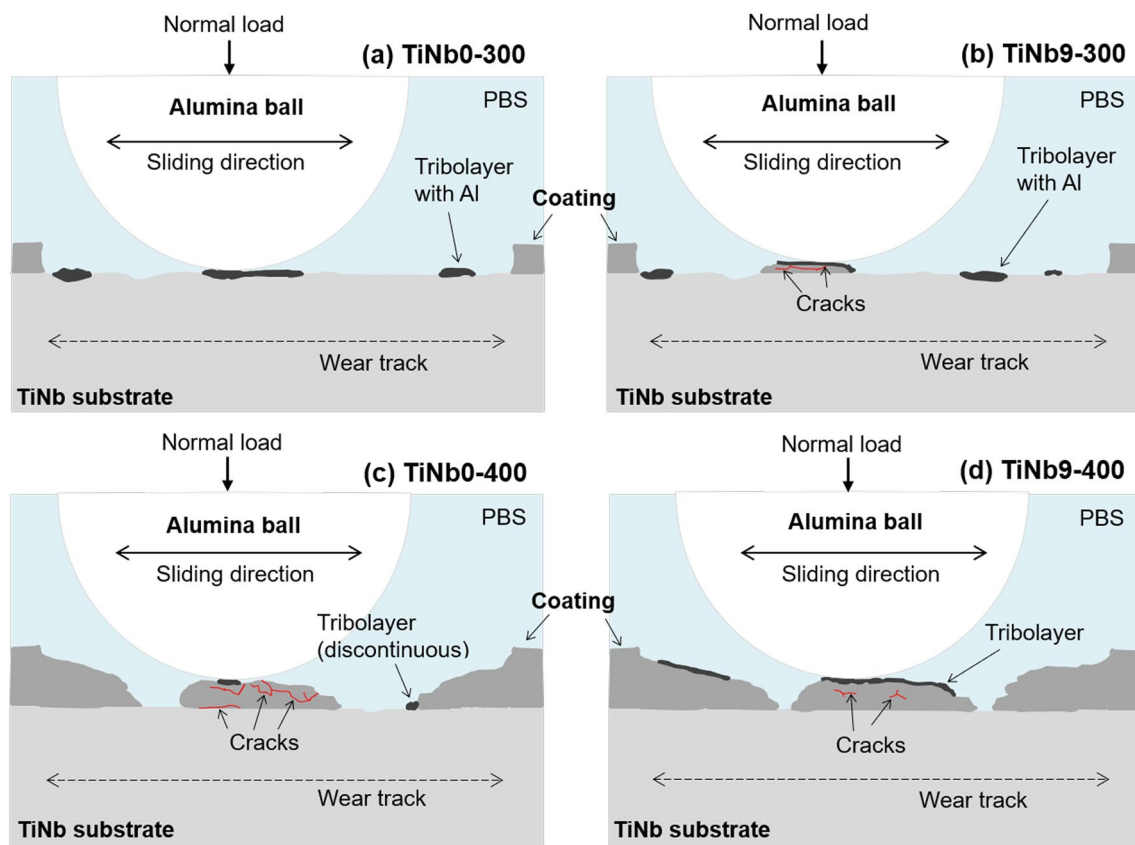
Fig. 15 Schematic illustration of the suggested tribocorrosion mechanisms of **a** TiNb0-300, **b** TiNb9-300, **c** TiNb0-400, and **d** TiNb9-400 samples

As only OCP measurements were carried out, no information on the rate of the corrosion reactions neither on the synergism between wear and corrosion phenomena is provided in this work. Therefore, further experiments should be conducted under potentiostatic conditions to quantify the corrosion current released from the material during mechanical actions. Furthermore, as future work, it would be of upmost importance to address potentiodynamic polarization analysis and electrochemical impedance spectroscopy (EIS), in order to extract detailed information on the corrosion mechanisms of those anodic coatings, bringing new understanding of the role of ZrO_2 NPs distributed along the MAO layers. An in-depth tribocorrosion investigation is needed, performing wear volume measurements and, especially, trying to simulate more closely the clinical environment where proteins are also present in the body fluids. Finally, a new study design is being drawn and applied in the tribocorrosion tests, considering both the porous nature of the contacting surfaces (MAO coating and bone) and the conditions of osseointegration well established after implantation.

5 Conclusions

Ti-40Nb alloy substrates were coated by MAO at different voltages in order to develop bio-functionalized surfaces incorporated with ZrO_2 NPs. Oxide growth mechanisms, incorporation of NPs, and tribocorrosion behavior were discussed. Within the limitations of this work, the main outcomes can be summarized as follows:

– Regardless the processing voltage and addition of ZrO_2 NPs, all coatings were incorporated with multiple bio-active species, as well, presented a multi-scale porous surface and a cross-section with triplex structure (barrier film, inner porous layer, and outer porous layer)
– An inert incorporation of ZrO_2 NPs was proposed to be a combined effect of electrophoresis and strong micro-arcs and discharges originated during MAO treatment. Higher processing voltage seems to improve that incorporation
– An enhanced incorporation of ZrO_2 NPs was shown to provide a better tribological behavior to the grown

oxide coating, possibly retarding eventual phenomena of brittleness and cracking associated with harder materials (rutile) under vigorous mechanical solicitations

Compliance with Ethical Standards

Conflict of Interest On behalf of all authors, the corresponding author states that there is no conflict of interest.

References

1. Kurtz S, Ong K, Lau E et al (2007) Projections of primary and revision hip and knee arthroplasty in the United States from 2005 to 2030. J Bone J Surg 89:780–785. https://doi.org/10.2106/JBJS.F.00222
2. Curtis EM, Moon RJ, Harvey NC, Cooper C (2017) The impact of fragility fracture and approaches to osteoporosis risk assessment worldwide. Bone 104:29–38. https://doi.org/10.1016/j.bone.2017.01.024
3. Waugh EJ, Badley EM, Borkhoff CM et al (2016) Primary care physicians' perceptions about and confidence in deciding which patients to refer for total joint arthroplasty of the hip and knee. Osteoarthr Cartil 24:451–457. https://doi.org/10.1016/j.joca.2015.09.017
4. Amirhosseini M, Andersson G, Aspenberg P, Fahlgren A (2017) Mechanical instability and titanium particles induce similar transcriptomic changes in a rat model for periprosthetic osteolysis and aseptic loosening. Bone Rep 7:17–25. https://doi.org/10.1016/j.bonr.2017.07.003
5. Clohisy JC, Calvert G, Tull F et al (2004) Reasons for revision hip surgery: A retrospective review. Clin Orthop Relat Res. https://doi.org/10.1097/01.blo.0000150126.73024.42
6. Dalury DF, Pomeroy DL, Gorab RS, Adams MJ (2013) Why are total knee arthroplasties being revised? J Arthroplasty 28:120–121. https://doi.org/10.1016/j.arth.2013.04.051
7. Bahraminasab M, Sahari BB, Edwards KL et al (2012) Aseptic loosening of femoral components: a review of current and future trends in materials used. Mater Des 42:459–470. https://doi.org/10.1016/j.matdes.2012.05.046
8. Chen Q, Thouas GA (2015) Metallic implant biomaterials. Mater Sci Eng R 87:1–57. https://doi.org/10.1016/j.mser.2014.10.001
9. Mathew MT, Srinivasa Pai P, Pourzal R et al (2009) Significance of tribocorrosion in biomedical applications: overview and current status. Adv Tribol. https://doi.org/10.1155/2009/250986
10. Toptan F, Alves AC, Pinto AMP, Ponthiaux P (2017) Tribocorrosion behavior of bio-functionalized highly porous titanium. J Mech Behav Biomed Mater 69:144–152. https://doi.org/10.1016/j.jmbbm.2017.01.006
11. Toptan F, Rego A, Alves AC, Guedes A (2016) Corrosion and tribocorrosion behavior of Ti-B4C composite intended for orthopaedic implants. J Mech Behav Biomed Mater 61:152–163. https://doi.org/10.1016/j.jmbbm.2016.01.024
12. Niinomi M, Liu Y, Nakai M et al (2016) Biomedical titanium alloys with Young's moduli close to that of cortical bone. Regen Biomater 3:173–185. https://doi.org/10.1093/rb/rbw016
13. Cordeiro JM, Barão VAR (2017) Is there scientific evidence favoring the substitution of commercially pure titanium with titanium alloys for the manufacture of dental implants? Mater Sci Eng C 71:1201–1215. https://doi.org/10.1016/j.msec.2016.10.025
14. Asgharzadeh Shirazi H, Ayatollahi MR, Asnafi A (2017) To reduce the maximum stress and the stress shielding effect around a dental implant–bone interface using radial functionally graded biomaterials. Comput Methods Biomech Biomed Eng 20:750–759. https://doi.org/10.1080/10255842.2017.1299142
15. Zhang QH, Cossey A, Tong J (2016) Stress shielding in periprosthetic bone following a total knee replacement: effects of implant material, design and alignment. Med Eng Phys 38:1481–1488. https://doi.org/10.1016/j.medengphy.2016.09.018
16. Rahyussalim AJ, Marsetio AF, Saleh I et al (2016) The needs of current implant technology in orthopaedic prosthesis biomaterials application to reduce prosthesis failure rate. J Nanomater. https://doi.org/10.1155/2016/5386924
17. Shah FA, Thomsen P, Palmquist A (2019) Osseointegration and current interpretations of the bone-implant interface. Acta Biomater 84:1–15. https://doi.org/10.1016/j.actbio.2018.11.018
18. Spriano S, Yamaguchi S, Baino F, Ferraris S (2018) A critical review of multifunctional titanium surfaces: new frontiers for improving osseointegration and host response, avoiding bacteria contamination. Acta Biomater 79:1–22. https://doi.org/10.1016/j.actbio.2018.08.013
19. Revathi A, Borrás AD, Muñoz AI et al (2017) Degradation mechanisms and future challenges of titanium and its alloys for dental implant applications in oral environment. Mater Sci Eng C 76:1354–1368. https://doi.org/10.1016/j.msec.2017.02.159
20. Zhang D, Wong CS, Wen C, Li Y (2017) Cellular responses of osteoblast-like cells to 17 elemental metals. J Biomed Mater Res A 105:148–158. https://doi.org/10.1002/jbm.a.35895
21. Lee CM, Ju CP, Chern Lin JH (2002) Structure-property relationship of cast Ti-Nb alloys. J Oral Rehabil 29:314–322. https://doi.org/10.1046/j.1365-2842.2002.00825.x
22. Bai Y, Deng Y, Zheng Y et al (2016) Characterization, corrosion behavior, cellular response and in vivo bone tissue compatibility of titanium-niobium alloy with low Young's modulus. Mater Sci Eng C 59:565–576. https://doi.org/10.1016/j.msec.2015.10.062
23. Alves AC, Wenger F, Ponthiaux P et al (2017) Corrosion mechanisms in titanium oxide-based films produced by anodic treatment. Electrochim Acta 234:16–27. https://doi.org/10.1016/j.electacta.2017.03.011
24. Alves SA, Bayón R, de Viteri VS et al (2015) Tribocorrosion behavior of calcium- and phosphorous-enriched titanium oxide films and study of osteoblast interactions for dental implants. J Bio Tribo Corros. https://doi.org/10.1007/s40735-015-0023-y
25. da Marques I, SV, Alfaro MF, Cruz NC da, et al (2016) Tribocorrosion behavior of biofunctional titanium oxide films produced by micro-arc oxidation: synergism and mechanisms. J Mech Behav Biomed Mater 60:8–21. https://doi.org/10.1016/j.jmbbm.2015.12.030
26. Felgueiras HP, Castanheira L, Changotade S et al (2015) Biotribocorrosion (tribo-electrochemical) characterization of anodized titanium biomaterial containing calcium and phosphorus before and after osteoblastic cell culture. J Biomed Mater Res B 103B:661–669. https://doi.org/10.1002/jbm.b.33236
27. Oliveira FG, Ribeiro AR, Perez G et al (2015) Understanding growth mechanisms and tribocorrosion behaviour of porous TiO2 anodic films containing calcium, phosphorous and magnesium. Appl Surf Sci 341:1–12. https://doi.org/10.1016/j.apsusc.2015.02.163

28. Yu JM, Choe HC (2019) Morphology changes and bone formation on PEO-treated Ti-6Al-4V alloy in electrolyte containing Ca, P, Sr, and Si ions. Appl Surf Sci 477:121–130. https://doi.org/10.1016/j.apsusc.2017.11.223

29. Wu SD, Zhang H, Dong XD et al (2015) Physicochemical properties and in vitro cytocompatibility of modified titanium surfaces prepared via micro-arc oxidation with different calcium concentrations. Appl Surf Sci 329:347–355. https://doi.org/10.1016/j.apsusc.2014.12.039

30. Ribeiro AR, Oliveira F, Boldrini LC et al (2015) Micro-arc oxidation as a tool to develop multifunctional calcium-rich surfaces for dental implant applications. Mater Sci Eng C 54:196–206. https://doi.org/10.1016/j.msec.2015.05.012

31. Zhao QM, Cheng L, Liu ZT, Zhao JJ (2014) Surface characteristics of Zinc-TiO$_2$ coatings prepared via micro-arc oxidation. Compos Interf 21:585–593. https://doi.org/10.1080/15685543.2014.914377

32. Yan J, Sun JF, Chu PK et al (2013) Bone integration capability of a series of strontium-containing hydroxyapatite coatings formed by micro-arc oxidation. J Biomed Mater Res A 101A:2465–2480. https://doi.org/10.1002/jbm.a.34548

33. Zhang Z (2015) Osteoblastic cell adhesion on Strontium-incorporated porous nanostructured TiO$_2$ coating prepared by micro-arc oxidation. J Clin Exp Orthop 01:1–6. https://doi.org/10.4172/2471-8416.100007

34. Okuzu Y, Fujibayashi S, Yamaguchi S et al (2017) Strontium and magnesium ions released from bioactive titanium metal promote early bone bonding in a rabbit implant model. Acta Biomater 63:383–392. https://doi.org/10.1016/j.actbio.2017.09.019

35. Sato M, Chen P, Tsutsumi Y et al (2016) Effect of strontium ions on calcification of preosteoblasts cultured on porous calcium-and phosphate-containing titanium oxide layers formed by micro-arc oxidation. Dent Mater J 35:627–634. https://doi.org/10.4012/dmj.2016-032

36. Gebert A, Eigel D, Gostin PF et al (2016) Oxidation treatments of beta-type Ti-40Nb for biomedical use. Surf Coat Technol 302:88–99. https://doi.org/10.1016/j.surfcoat.2016.05.036

37. Lu X, Mohedano M, Blawert C et al (2016) Plasma electrolytic oxidation coatings with particle additions: a review. Surf Coatings Technol 307:1165–1182. https://doi.org/10.1016/j.surfcoat.2016.08.055

38. Gowtham S, Hariprasad S, Arunnellaiappan T, Rameshbabu N (2017) An investigation on ZrO$_2$ nano-particle incorporation, surface properties and electrochemical corrosion behaviour of PEO coating formed on Cp-Ti. Surf Coatings Technol 313:263–273. https://doi.org/10.1016/j.surfcoat.2017.01.105

39. Lee KM, Lee BU, Il YS et al (2012) Evaluation of plasma temperature during plasma oxidation processing of AZ91 Mg alloy through analysis of the melting behavior of incorporated particles. Electrochim Acta 67:6–11. https://doi.org/10.1016/j.electacta.2012.01.053

40. Lee KM, Shin KR, Namgung S et al (2011) Electrochemical response of ZrO$_2$-incorporated oxide layer on AZ91 Mg alloy processed by plasma electrolytic oxidation. Surf Coatings Technol 205:3779–3784. https://doi.org/10.1016/j.surfcoat.2011.01.033

41. Arrabal R, Matykina E, Skeldon P, Thompson GE (2008) Incorporation of zirconia particles into coatings formed on magnesium by plasma electrolytic oxidation. J Mater Sci 43:1532–1538. https://doi.org/10.1007/s10853-007-2360-9

42. Arrabal R, Matykina E, Viejo F et al (2008) AC plasma electrolytic oxidation of magnesium with zirconia nanoparticles. Appl Surf Sci 254:6937–6942. https://doi.org/10.1016/j.apsusc.2008.04.100

43. Gnedenkov SV, Sinebryukhov SL, Mashtalyar DV et al (2015) Fabrication of coatings on the surface of magnesium alloy by plasma electrolytic oxidation using ZrO$_2$ and SiO$_2$ nanoparticles. J Nanomater. https://doi.org/10.1155/2015/154298

44. Rehman ZU, Shin SH, Lim HT, Koo BH (2017) Transformation of plasma electrolytic oxidation coatings from crater to cluster–based structure with increase in DC voltage and the role of ZrO$_2$ nanoparticles. Surf Coatings Technol 311:383–390. https://doi.org/10.1016/j.surfcoat.2016.12.112

45. Mohedano M, Arrabal R, Mingo B et al (2018) Role of particle type and concentration on characteristics of PEO coatings on AM50 magnesium alloy. Surf Coatings Technol 334:328–335. https://doi.org/10.1016/j.surfcoat.2017.11.058

46. Matykina E, Arrabal R, Monfort F et al (2008) Incorporation of zirconia into coatings formed by DC plasma electrolytic oxidation of aluminium in nanoparticle suspensions. Appl Surf Sci 255:2830–2839. https://doi.org/10.1016/j.apsusc.2008.08.036

47. Matykina E, Arrabal R, Skeldon P, Thompson GE (2008) Incorporation of zirconia nanoparticles into coatings formed on aluminium by AC plasma electrolytic oxidation. J Appl Electrochem 38:1375–1383. https://doi.org/10.1007/s10800-008-9575-6

48. Hu CJ, Hsieh MH (2014) Preparation of ceramic coatings on an Al-Si alloy by the incorporation of ZrO$_2$ particles in micro-arc oxidation. Surf Coatings Technol 258:275–283. https://doi.org/10.1016/j.surfcoat.2014.09.012

49. Arunnellaiappan T, Arun S, Hariprasad S et al (2018) Fabrication of corrosion resistant hydrophobic ceramic nanocomposite coatings on PEO treated AA7075. Ceram Int 44:874–884. https://doi.org/10.1016/j.ceramint.2017.10.014

50. Shin KR, Ko YG, Shin DH (2012) Surface characteristics of ZrO$_2$-containing oxide layer in titanium by plasma electrolytic oxidation in K$_4$P$_2$O$_7$ electrolyte. J Alloys Compd 536S:S226–S230. https://doi.org/10.1016/j.jallcom.2011.11.037

51. Shin KR, Kim YS, Kim GW et al (2015) Development of titanium oxide layer containing nanocrystalline zirconia particles with tetragonal structure: structural and biological characteristics. Colloids Surf B 131:47–53. https://doi.org/10.1016/j.colsurfb.2015.03.047

52. Li H, Sun Y, Zhang J (2015) Effect of ZrO$_2$ particle on the performance of micro-arc oxidation coatings on Ti$_6$Al$_4$V. Appl Surf Sci 342:183–190. https://doi.org/10.1016/j.apsusc.2015.03.051

53. Abdi S, Khoshkhoo MS, Shuleshova O et al (2014) Effect of Nb addition on microstructure evolution and nanomechanical properties of a glass-forming Ti-Zr-Si alloy. Intermetallics 46:156–163. https://doi.org/10.1016/j.intermet.2013.11.010

54. Yoshida H, Faust A, Wilckens J et al (2006) Three-dimensional dynamic hip contact area and pressure distribution during activities of daily living. J Biomech 39:1996–2004. https://doi.org/10.1016/j.jbiomech.2005.06.026

55. Sharma A, Komistek RD, Ranawat CS et al (2007) In vivo contact pressures in total knee arthroplasty. J Arthroplasty 22:404–416. https://doi.org/10.1016/j.arth.2006.07.008

56. Alves AC, Costa AI, Toptan F et al (2020) Effect of bio-functional MAO layers on the electrochemical behaviour of highly porous Ti. Surf Coatings Technol 386:125487. https://doi.org/10.1016/j.surfcoat.2020.125487

57. Çaha I, Alves AC, Affonço LJ et al (2019) Corrosion and tribocorrosion behaviour of titanium nitride thin films grown on titanium under different deposition times. Surf Coatings Technol 374:878–888. https://doi.org/10.1016/j.surfcoat.2019.06.073

58. Correa DRN, Kuroda PAB, Grandini CR et al (2016) Tribocorrosion behavior of β-type Ti-15Zr-based alloys. Mater Lett 179:118–121. https://doi.org/10.1016/j.matlet.2016.05.045

59. Alves SA, Rossi AL, Ribeiro AR et al (2018) Improved tribocorrosion performance of bio-functionalized TiO$_2$ nanotubes under two-cycle sliding actions in artificial saliva. J Mech Behav Biomed Mater 80:143–154. https://doi.org/10.1016/j.jmbbm.2018.01.038

60. Costa AI, Sousa L, Alves AC, Toptan F (2020) Tribocorrosion behaviour of bio-functionalized porous Ti surfaces obtained by two-step anodic treatment. Corros Sci 166:108467. https://doi.org/10.1016/j.corsci.2020.108467

61. Mazzarolo A, Curioni M, Vicenzo A et al (2012) Anodic growth of titanium oxide: electrochemical behaviour and morphological evolution. Electrochim Acta 75:288–295. https://doi.org/10.1016/j.electacta.2012.04.114

62. Pan Y-N, Lin C-S, Wang K-K, Ou S-F (2014) Effect of Nb addition on anodic behavior of Ti alloy in electrolyte containing calcium and phosphorus. Surf Coatings Technol 258:1016–1024. https://doi.org/10.1016/j.surfcoat.2014.07.037

63. Wang Y, Yu H, Chen C, Zhao Z (2015) Review of the biocompatibility of micro-arc oxidation coated titanium alloys. Mater Des 85:640–652. https://doi.org/10.1016/j.matdes.2015.07.086

64. Sowa M, Worek J, Dercz G et al (2016) Surface characterisation and corrosion behaviour of niobium treated in a Ca- and P-containing solution under sparking conditions. Electrochim Acta 198:91–103. https://doi.org/10.1016/j.electacta.2016.03.069

65. Kuromoto NK, Simão RA, Soares GA (2007) Titanium oxide films produced on commercially pure titanium by anodic oxidation with different voltages. Mater Charact 58:114–121. https://doi.org/10.1016/j.matchar.2006.03.020

66. Cengiz S, Azakli Y, Tarakci M et al (2017) Microarc oxidation discharge types and bio properties of the coating synthesized on zirconium. Mater Sci Eng C 77:374–383. https://doi.org/10.1016/j.msec.2017.03.230

67. Arun S, Arunnellaiappan T, Rameshbabu N (2016) Fabrication of the nanoparticle incorporated PEO coating on commercially pure zirconium and its corrosion resistance. Surf Coatings Technol 305:264–273. https://doi.org/10.1016/j.surfcoat.2016.07.086

68. Venkateswarlu K, Rameshbabu N, Chandra Bose A et al (2012) Fabrication of corrosion resistant, bioactive and antibacterial silver substituted hydroxyapatite/titania composite coating on Cp Ti. Ceram Int 38:731–740. https://doi.org/10.1016/j.ceramint.2011.07.065

69. Necula BS, Apachitei I, Tichelaar FD et al (2011) An electron microscopical study on the growth of TiO_2-Ag antibacterial coatings on Ti_6Al_7Nb biomedical alloy. Acta Biomater 7:2751–2757. https://doi.org/10.1016/j.actbio.2011.02.037

70. Lu X, Blawert C, Zheludkevich ML, Kainer KU (2015) Insights into plasma electrolytic oxidation treatment with particle addition. Corros Sci 101:201–207. https://doi.org/10.1016/j.corsci.2015.09.016

71. Ponthiaux P, Wenger F, Drees D, Celis JP (2004) Electrochemical techniques for studying tribocorrosion processes. Wear 256:459–468. https://doi.org/10.1016/S0043-1648(03)00556-8

72. Costa AI, Viana F, Toptan F (2021) Preliminary tribocorrosion evaluation of bio-functionalized Ti doped with Ca-P-Sr. Mater Lett 283:128775. https://doi.org/10.1016/j.matlet.2020.128775